TOPICAL REVIEW

Attosecond light sources in the water window

View the article online for updates and enhancements.

Topical Review

Attosecond light sources in the water window

Xiaoming Ren[1]**, Jie Li**[1]**, Yanchun Yin**[1] **, Kun Zhao**[2]**, Andrew Chew**[1]**, Yang Wang**[1]**, Shuyuan Hu**[1]**, Yan Cheng**[1]**, Eric Cunningham**[1]**, Yi Wu**[1]**, Michael Chini**[3] **and Zenghu Chang**[1,3]

[1] Institute for the Frontier of Attosecond Science and Technology, CREOL, University of Central Florida, Orlando, FL 32816, United States of America
[2] Beijing National Laboratory for Condensed Matter Physics, Institute of Physics, Chinese Academy of Sciences, Beijing 100190, People's Republic of China
[3] Department of Physics, University of Central Florida, Orlando, FL 32816, United States of America

E-mail: Zenghu.Chang@ucf.edu

Abstract

As a compact and burgeoning alternative to synchrotron radiation and free-electron lasers, high harmonic generation (HHG) has proven its superiority in static and time-resolved extreme ultraviolet spectroscopy for the past two decades and has recently gained many interests and successes in generating soft x-ray emissions covering the biologically important water window spectral region. Unlike synchrotron and free-electron sources, which suffer from relatively long pulse width or large time jitter, soft x-ray sources from HHG could offer attosecond time resolution and be synchronized with their driving field to investigate time-resolved near edge absorption spectroscopy, which could reveal rich structural and dynamical information of the interrogated samples. In this paper, we review recent progresses on generating and characterizing attosecond light sources in the water window region. We show our development of an energetic, two-cycle, carrier-envelope phase stable laser source at 1.7 μm and our achievement in producing a 53 as soft x-ray pulse covering the carbon K-edge in the water window. Such source paves the ways for the next generation x-ray spectroscopy with unprecedented temporal resolution.

Keywords: high harmonic generation, attosecond laser, water window x-ray, attosecond laser characterization

(Some figures may appear in colour only in the online journal)

1. Introduction

High harmonic generation (HHG), a coherent burst of high energy photons with photon energy up-converted from its driving field, has enabled table-top extreme ultraviolet (XUV) and x-ray lasers and most importantly spawned the attosecond science [1, 2]. Its superior temporal characteristics as compared to synchrotron and free electron sources have made it a unique tool for studying time resolved spectroscopy in a photon energy range of a few eV to well above 1 keV. The

first generation attosecond light sources, enabled by Ti:sapphire lasers, usually have access to photon energies below 150 eV. From a single atom point of view, the maximum HHG photon energy is given by $E_{\mathrm{cutoff}} = I_p + 3.17 U_p$, where I_p is the ionization potential of the gas target and $Up \propto I_L \lambda_L^2$ is the quiver energy. To increase the cutoff photon energy, an easy way is to increase the laser intensity I_L by either increasing the pulse energy or decrease the pulse duration of the driving laser or using a tight focus. Under extreme conditions with strong ionization, the cutoff photon energy can be

Table 1. Cutoff photon energies that extend beyond carbon K-edge from various infrared laser systems.

Infrared laser systems	Generation gas	Cutoff energy (eV)	References
10 Hz, 1.3 μm, 5.5 mJ, 35 fs	Helium[a]	330	[5]
1 kHz, 1.5 μm, 1.6 mJ, 50 fs	Neon	400	[7]
1 kHz, 1.6 μm, 0.55 mJ, 9 fs	Neon	320	[8]
10 Hz, 1.6 μm, 2.2(4.5) mJ, 35 fs	Neon(Helium)	300(450)	[9]
1 kHz, 1.8 μm, 0.7 mJ, 8 fs	Neon	375	[10]
1 kHz, 1.85 μm, 0.4 mJ, 12 fs	Neon(Helium)	350(500)	[11]
10 Hz, 2 μm, 2.4 mJ, 40 fs	Neon(Helium)	395(520)	[12]
1 kHz, 2.1 μm, 1.35 mJ, 32 fs	Neon	450	[13]
20 Hz, 3.9 μm, 10 mJ, 80 fs	Helium[a]	1600	[14]

[a] Waveguide is used to achieve better phase matching at high photon energies.

extended [3] and reach as high as 460 eV [4] in helium with Ti:sapphire lasers. However, to generate bright high harmonic (HH) emissions requires microscopic phase matching. The driving laser and the HH need to propagate with the same phase velocity (speed of light) to insure the HH field emitted from different gas emitters add up coherently. While the high frequency HH field rarely interacts with the gas media and therefore maintains its phase velocity at speed of light. The propagation of the driving field is affected by the neutral gas and free-electron plasma as well as the laser focusing geometry [5]. Therefore, under strong ionization, the dense free-electron plasma which causes strong phase mismatch prevents the photon flux at these cutoff photon energies from practical uses.

The alternative way to scale up cutoff photon energy is to increase the driving laser wavelength λ_L [6]. Thanks to the rapid development of high energy, high repetition rate short/mid wavelength infrared laser systems in recent years, the second generation attosecond sources can now have access to photon energies that were previously only accessible to facility scale sources with sufficient photon flux. Water window source, lying in the soft x-ray region between the K-shell absorption edge of carbon (284 eV) and K-shell absorption edge of oxygen (543 eV), has especially attracted lots of interests due to its unique property of being transmissive to water and covering absorption edges of fundamental biological elements. Utilizing driving lasers with their center wavelengths ranging from 1.3 to 2.1 μm [5, 7–13] or even 3.9 μm [14], water window harmonics and attosecond continua have been generated with their photon energies well pass the carbon K-edge or even above 1 keV. Table 1 summaries the cutoff energies of existing water window sources from various infrared laser systems. These water window sources could be ideal tool for time-resolved near edge absorption spectroscopy of biological samples [15, 16] and allow probing fast excitation and ionization dynamics at the native time scale of the microscopic world.

Going from HH emissions to isolated attosecond pulses requires isolating these half-cycle processes either spatially [17] or temporally [18–23]. Both have been recently achieved in the water window region via wavefront rotation [24] and polarization gating (PG) [25]. However, the pulse characterization still faces great challenges. Although method based on

photon measurement has been proposed to measure the pulse duration [26], easier access to the phase information still requires photoelectron streaking measurement, where the extremely low photoelectron counts is the biggest obstacle of such measurement. As the driving laser wavelength becomes longer, the quiver energy scales quadratically with the wavelength, resulting in the higher photon energy up to the water window. With that comes the drastically reduced photo-recombination cross section, resulting in a HHG efficiency that drops as $\lambda_L^{-5\sim-6}$ [27]. Even though using higher gas pressure could mitigate such drop to some extent [5], increasing the HHG efficiency with long wavelength driving lasers is still an ongoing research of the field [28]. Isolating the water window attosecond pulse further reduces its photon flux by several times, depending on the cycle numbers of the driving laser. These isolated water window attosecond pulses then experience further reduction in flux by propagating through metallic filters, which are necessary for blocking fundamental light as well as compensating the intrinsic atto-chirp [29]. Lastly, the conversion from photons to photo-electrons, occurring in neon or helium gas which is essential for eliminating secondary processes upon absorbing a water window photon [30], has an extremely low cross-section, limiting the final electron detection to be much less than one event per laser shot. Thus, in order to fulfill a streaking measurement in the water window, a high repetition rate, high pulse energy, few-cycle long wavelength laser with long term carrier-envelope phase (CEP) stability is essential.

In this paper, we review recent progresses on attosecond pulse generation and characterization in the water window. For the generation, we review recent advances in achieving few-cycle CEP stable short/mid infrared driving lasers, and the resulted attosecond water window continua. For the characterization, we focus on our recent achievement of a 53 as water window source. PG CEP stable two-cycle pulses at 1.7 μm are used to generate soft x-ray continuum up to 300 eV, supporting a transform limited attosecond pulse with a duration of 20 as. The intrinsic atto-chirp of the attosecond pulse is then compensated by a series of Sn filters with different thickness. Photoelectron streaking measurement is realized for the first time in the water window region and measures an isolated attosecond pulse duration of 53 as when a 400 nm Sn filter is used [31]. The paper is organized as
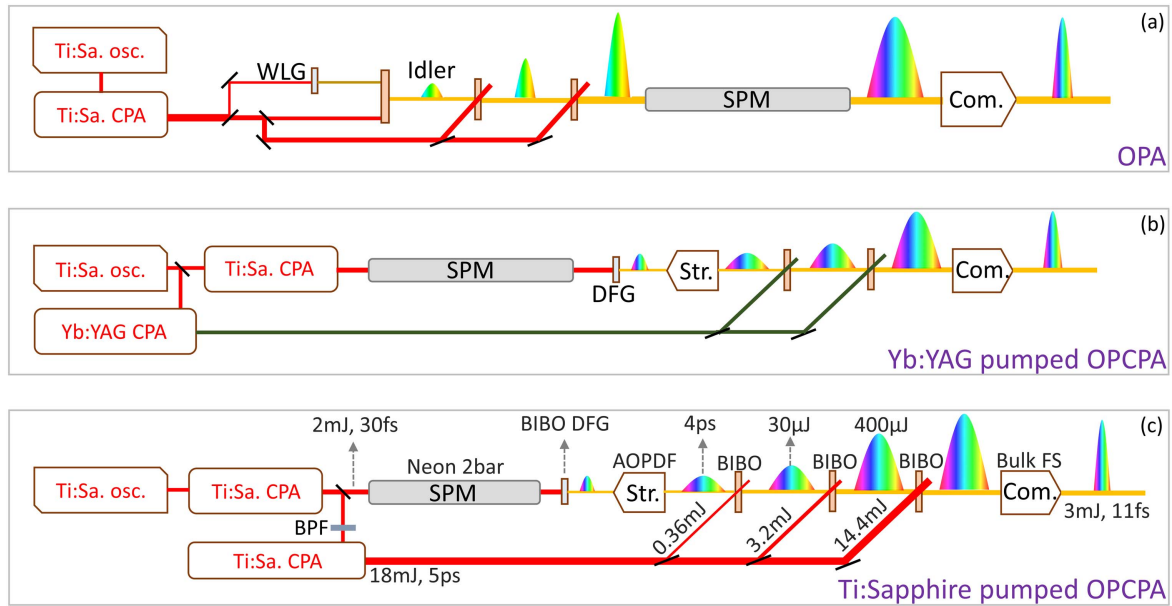
Figure 1. (a) Schematic setup of the few-cycle laser system based on OPA technique. (b) Schematic setup of the few-cycle laser system based on OPCPA technique with ps Yb:YAG laser as the pumping source. (c) Schematic setup of the few-cycle laser system based on OPCPA technique with chirped Ti:sapphire laser as the pumping source. WLG: white light generation. SPM: self-phase modulation. Com.: compressor. DFG: difference frequency generation. Str.: stretcher. BPF: band-pass filter. FS: fused silica.

follows: in section 2, we review recent progresses on generating few-optical-cycle short/mid infrared laser systems and describe in detail the design of our laser system. In section 3, we review state-of-art water window sources and the isolation of the water window attosecond pulses. We will show our PG technique along with the first photoelectron streaking measurement reaching the water window. In section 4, we review popular attosecond pulse retrieval methods and explain our phase retrieval technique and retrieved results. In section 5, we review recent progresses on time resolved studies near carbon K-absorption edge and show the possibility of applying our water window source for a time resolved near edge absorption experiment with better temporal resolution. In section 6, we review recent achievements on developing mid-infrared laser systems and propose new designs of such lasers for generating even higher photon energies, and finally, we conclude in section 7.

2. Driving laser

In order to develop a high pulse energy, few-cycle long wavelength laser with CEP stability, a seed laser with broad bandwidth and CEP stability is needed first. Seed lasers with these characteristics are readily achievable using techniques such as difference frequency generation (DFG), four-wave mixing and white light generation (WLG), providing octave/near octave spanning μJ energy level seed lasers with their bandwidth covering, for instance, from 1.2 to 2.2 μm [32, 33], 1.5 to 3 μm [34], 1.7 to 4 μm [35] and 2 to 6 μm [36]. Amplifying those seed lasers to mJ level pulse energy can then employ one of the three conventional amplification techniques, namely chirped-pulse amplification (CPA),

optical parametric amplification (OPA) and optical parametric CPA (OPCPA).

CPA requires specific gain material and pump source, transition metal doped II-VI semiconductors such as Cr^{2+}:ZnSe/Cr^{2+}:ZnS and Fe^{2+}:ZnSe/Fe^{2+}:ZnS are promising gain materials for amplifying the desired spectrum, which have very broad gain bandwidth covering 1.9–3.4 μm and 3.4–6 μm, respectively [37]. However, such laser systems are relatively immature and face challenges on thermal management and only provide multi-cycle pulses due to gain narrowing effect.

OPA is known to suffer much less thermal problem and have a very broad tuning range. A typical few-cycle laser system based on OPA technique is depicted in figure 1(a). The CEP stable broadband seed laser is generated in the initial stage by doing DFG (normally in a BBO crystal) between a small portion of the Ti:sapphire laser and its WLG. Due to the temporal chirp in WLG, by changing the delay between the pump and signal, and the phase matching angle of the nonlinear crystal, idler pulses centered at 1.6–2 μm can be achieved and amplified to mJ level in two or more OPA stages. However, limited bandwidth is generated due to the initial chirp in the WLG, resulting in multi-cycle laser pulses at the exit of the OPA. Therefore, subsequent spectral broadening techniques such as self-phase modulation (SPM) in gas filled hollow-core fiber need to be employed to achieve octave-spanning spectra, which are then compressed to few-cycle pulse durations taking advantage of the anomalous dispersion of bulk materials in the desired spectral range. Several research groups have adopted this design and achieved near mJ level CEP stable laser with less than two-cycle pulse duration [10, 38, 39]. Water window attosecond continua have also successfully been demonstrated using such

lasers. However, the energy scalability of such laser is limited by the availability of large size crystals for OPA and the low damage threshold of the fiber and its low efficiency.

OPCPA has proven its superiority in scaling up the output energy and amplifying octave spanning spectra. A popular design is depicted in figure 1(b), a Ti:sapphire front-end is used to generate octave spanning seed laser for the OPCPA and at the same time seed a ps high energy pump laser, in this case a Yb:YAG CPA system. The seed laser is then stretched to ps duration and amplified by the pump laser to mJ level pulse energy in a few amplification stages. The octave spanning spectrum is preserved in the process and compressed to few-cycle pulse duration using bulk materials at the end. Employing this technique, Deng *et al* [34] reported a 3 kHz, 1.2 mJ, 10.5 fs, CEP stable laser centered at 2.1 μm in PPLN pumped by Yb:YAG thin disc laser; Hong *et al* [40] achieved a 1 kHz, 2.6 mJ, 40 fs, CEP stable laser centered at 2.1 μm in PPLN pumped by Yb:YAG laser. Another new OPCPA design based purely on Ti:sapphire lasers is shown in figure 1(c). Different from aforementioned OPCPA design, the pump source in this design is also a Ti:sapphire laser with its output pulse chirped to a few ps. The chirp of the seed and pump laser is carefully matched to amplify the octave spanning seed laser and provide a mJ level few-cycle laser pulse after a few amplification stages and pulse compression. Following this design, Ishii *et al* [32] demonstrated a 1 kHz, 0.55 mJ, 9 fs, CEP stable laser centered at 1.6 μm in BIBO crystals, later upgraded to 1.5 mJ [41]; we also reported a 1 kHz, 3 mJ, 11 fs, CEP stable laser centered at 1.7 μm in BIBO crystals [33]. The much higher pulse energy is the result of our development of a high energy Ti:sapphire laser system and its tailored spectrum for achieving higher conversion efficiency. These state-of-art OPCPA systems have successfully extended the HHG cutoff into the water window with sufficient photon flux [8, 13, 25] and are the key to the next generation water window attosecond sources. Our laser design is briefly described as follows.

As illustrated in figure 1(c), part of our home-built Ti: sapphire laser system is used for few-cycle pulse generation in a 1.5 m long, 550 μm inner core hollow-core fiber filled with 2 bar neon gas, followed by intra-pulse DFG in a Type-II BIBO crystal (phase matching angle $\theta = 60°$), the generated broadband pulses are stretched by an acousto-optic programmable dispersive filter (AOPDF) (Fastlite) to around 4 ps to serve as the seed for the OPCPA. The rest of the high power Ti:sapphire pulses are chirped to 5 ps and spectrally filtered to within 760 and 810 nm to serve as the pump for the OPCPA, this particular bandwidth is chosen to maximize the efficiency of the OPCPA [33]. Then the seed pulses are amplified to 3 mJ in a three-stage OPCPA consisting of three type-I BIBO crystals with a phase matching angle of $\theta = 10.8°$ and a small noncolinear angle of $\alpha = 0.6°$. Finally, the output is compressed in a 150 mm long infrared fused silica bulk compressor and the spectral phase is fine tuned by the AOPDF to achieve a pulse duration of 11.4 fs as measured by a home-built second harmonic generation frequency resolved optical gating (SHG FROG). The results are depicted in figure 2(C). For comparison, FROG measurements of the

few-cycle pulses achieved via the designs in figure 1(a) [39] and figure 1(b) [34] are also shown in figures 2(A) and (B), respectively.

To verify the passive CEP stability of the system originated from the DFG process [42], a small portion of the output laser is focused into a 1mm sapphire plate for WLG and the broadened spectrum is frequency doubled to form a f-2f interferogram. The single-shot f-2f fringe accumulated for 1 h and the corresponding CEP values are shown in figure 2(D), indicating a CEP fluctuation of 165 mrad (root-mean-square value) without any active feedback. This excellent long term CEP stability is essential for achieving successful photoelectron streaking measurement, which will be elaborated in the following section.

3. Generation and characterization of isolated attosecond pulses in the water window

Figure 3 depicts our experimental setup to generate and characterize isolated attosecond pulses in the water window. For the generation part, PG optics are used to isolate attosecond pulses, which could be substituted with other techniques such as wavefront rotation. The source of the generation gas is also not limited to gas cells, other popular sources such as semi-infinite gas cell or gas jet can be employed as long as they can provide sufficient pressure-length product. The spectra of the attosecond pulses are detected using standard soft x-ray spectrometer. For the characterization part, photoelectrons are collected using magnetic bottle electron time of flight (TOF) spectrometer [43, 44], other standard TOF spectrometers based on charged plates are more commonly employed with a slightly lower collection efficiency. A fully collinear setup without beam splitting is also widely used for the streaking measurement, however the bandwidth of the streaked attosecond pulses is limited by the reflection bandwidth of the multi-layer mirror [45] and so far is not applicable for characterizing water window attosecond pulses. In the following subsections, progresses on both parts will be reviewed and explained in detail.

3.1. Generating isolated attosecond pulses in the water window

As elaborated in the introduction, going from HHG emission to isolated attosecond pulses requires sub-cycle gating techniques, since the ionization and recombination events that lead to the attosecond pulse emission happen at every half-cycle of the laser field. Even with two-cycle laser pulses, a train of attosecond pulses are produced [18]. Despite of its narrow bandwidth, the cutoff region could form an isolated attosecond pulse, this can be evidenced from its CEP dependence [8, 11]. Figure 4 shows the CEP dependence of the cutoff photon energy from [11]. It is clear that isolated attosecond pulses are generated near the cutoff region, but the bandwidth is limited. In order to generate an isolated attosecond pulse covering water window with broad bandwidth, which is important for studying multiple absorption lines at
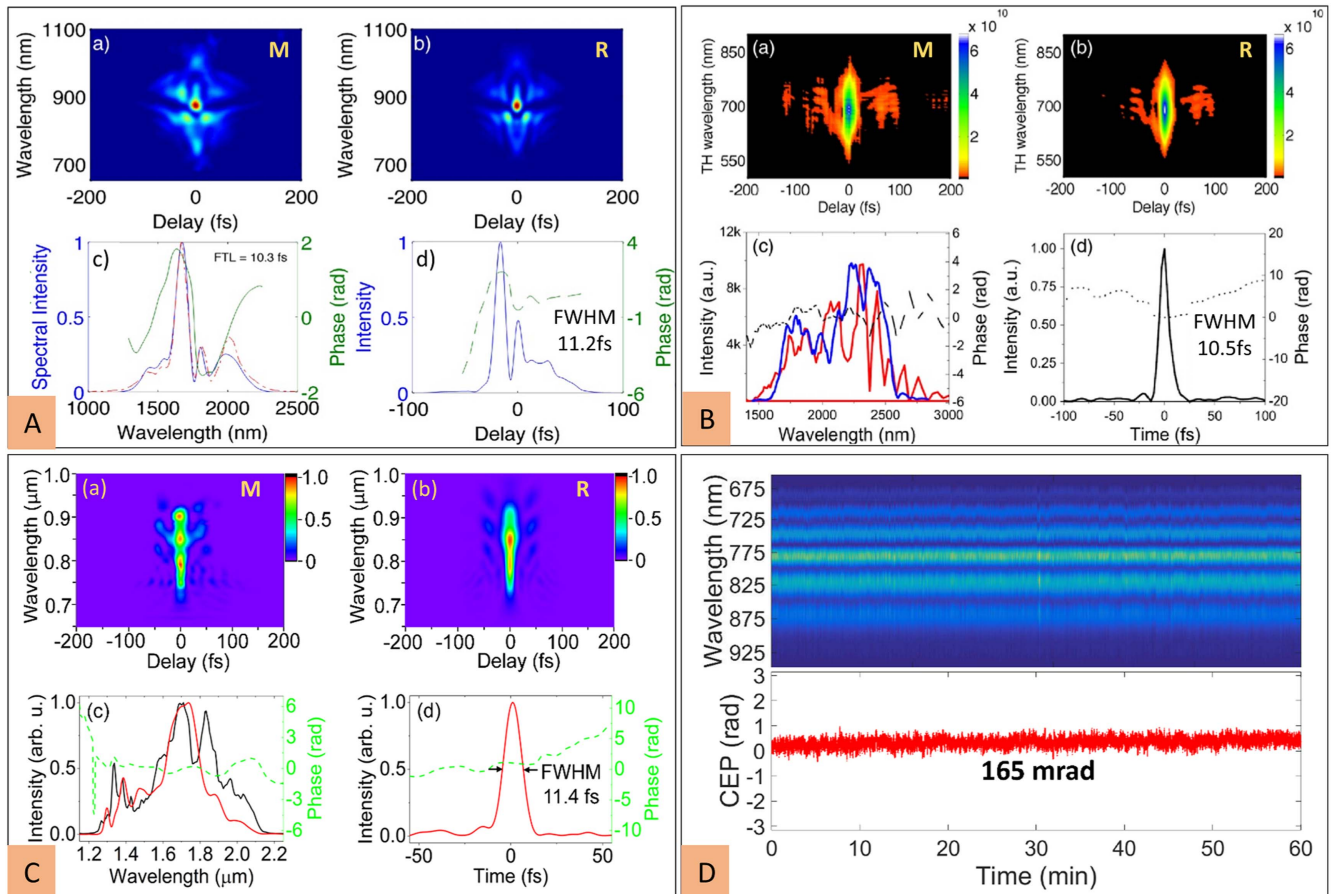
Figure 2. (A) FROG measurement of the few-cycle pulse achieved using the setup in figure 1(a). Reproduced with permission from [39]. (B) FROG measurement of the few-cycle pulse achieved using the setup in figure 1(b). Reproduced with permission from [34]. (C) FROG measurement of the few-cycle pulse achieved using the setup in figure 1(c). Reproduced with permission from [33]. In all figures: (A) measured SHG FROG trace; (B) retrieved SHG FROG trace; (C) measured spectrum, retrieved spectrum and retrieved spectral phase; (D) retrieved pulse temporal profile and temporal phase. (D) CEP measurement of our OPCPA output. Top: single-shot f-2f fringes collected for 1 h; bottom: relative CEP values extracted from the fringes, corresponding to a CEP fluctuation of 165 mrad in 1 h. Reproduced with permission from [33].
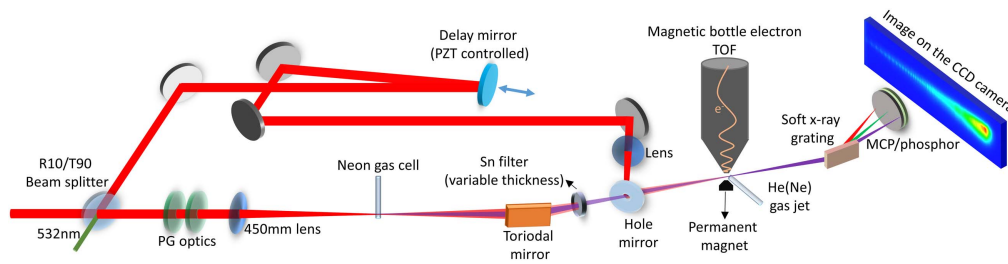

Figure 3. Our experimental setup for generating and characterizing isolated attosecond pulses. PG: polarization gating; TOF: time of flight; MCP: micro-channel plate

once and producing shorter attosecond pulses, sub-cycle gating techniques are needed. So far, two gating techniques that are widely used in the first generation attosecond sources have been extended to isolate water window attosecond pulses. Silva *et al* recently demonstrated spatiotemporal isolation of attosecond pulses in the water window using attosecond lighthouse [24]. Attosecond pulses within the pulse train are spatially separated as multiple beamlets that propagate at slightly different emission angles. By spatially selecting one beamlet, isolated attosecond pulse in the water window can be

obtained. Figure 5 shows the spectra of such pulses under three different CEP values, the lighthouse effect is clearly evidenced from the CEP dependent emission angles, although the bandwidth of the isolated attosecond pulse is still limited in this particular study.

Recently, we implemented the widely used PG technique to isolate attosecond pulses in the water window region [25]. The basic idea of PG using our 1.7 μm laser is detailed as follows: a quartz plate of 180 μm (379 μm) thickness is set with its optical axis aligned at 45° with respect to the input
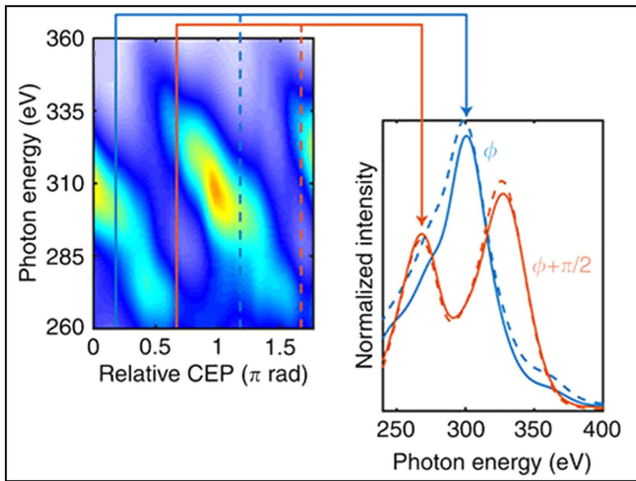
Figure 4. CEP dependent harmonic spectrum obtained with a 1 kHz, 1.85 μm, 0.4 mJ and 12 fs driving laser. Reproduced from [11]. CC BY 3.0.

laser polarization direction, thus introducing a delay Δt between the fast and slow axis projections of the input laser, with Δt corresponding to one- (two-) laser cycle delay. The subsequent quarter waveplate changes the two pulses into counter-rotating elliptically polarized pulses with a linearly polarized laser field in the overlapped region. The temporal duration of this linear portion is termed as the PG width $\delta t_G = \varepsilon_{th} \tau_p^2 / (\ln 2 \Delta t)$, where ε_{th} is the threshold ellipticity and is determined to be 0.1 [25], $\tau_p = 11.4$ fs is the pulse duration of our driving laser. When Δt is set at one- (two-) cycle delay, which is 5.6 fs (11.3 fs) for a 1.7 μm laser, the PG width is calculated to be $\delta t_G = 3.6$ fs (1.8 fs). While the attosecond pulse emission happens at every half-cycle of the laser field, a proper gate width that can ensure an isolated attosecond pulse should be less than half of the optical cycle, which is 2.8 fs. It is then apparent that the two-cycle gating should be chosen to generated isolated attosecond pulse under our laser condition. Note that a proper choice of CEP in the case of the one-cycle gating will also result in only one ionization and recombination event, as will be evidenced in later measurements.

The PG laser field is then focused by a 450 mm lens into a high pressure neon gas cell to generate attosecond continua. The gas cell is 1.5 mm long filled with 1 bar neon gas that is optimized for the cutoff photon energy as well as the photon flux. A pressure scan is shown in figure 6(a), revealing the generation of soft x-ray photons slightly above the carbon K-edge with a cutoff photon energy at around 300 eV. The reduction of the cutoff above 1 bar is due to the plasma defocusing of the driving laser that resulted in a decreased laser peak intensity. For comparison, pressure scan in [11] is shown in figure 6(b). A much higher cutoff is obtained by tightening the focusing of the driving laser, in this case using a 100 mm spherical mirror. As shown in figure 3, the generated attosecond pulses are focused by a toroidal mirror into a second gas target for photoelectron generation, which will be discussed in the following section. A series of Sn filters with various thickness are inserted into the beam to block the

fundamental laser as well as to compensate for the intrinsic atto-chirp. Starting from the second gas target, a soft x-ray imaging spectrometer is constructed to detect the spectrum of the generated attosecond pulse, consisting of a 1200 line mm^{-1} laminar-type soft x-ray diffraction grating (Shimadzu 03-005), a micro-channel plate backed with a phosphor screen and a cooled CCD camera. The measured spectra with a linear pulse, a one-cycle gated pulse and a two-cycle gated pulse are compared in figure 6(c). Even though the two-cycle gating provides the best PG width for the isolation of the attosecond pulses, it sacrifices about five times and over one order of magnitude on the photon flux compared to the one-cycle gating and linear cases, respectively.

Due to the limited spectral resolution of our spectrometer near the cutoff region, it is hard to justify the isolation of the attosecond pulses from the continuous spectrum. CEP dependent spectra are therefore measured under the three different schemes to better prove the generation of the isolated attosecond pulses, since only the spectra from the isolated attosecond pulses exhibit strong CEP dependence. The measurements are shown in figure 7. In the case of the linearly polarized pulses, the CEP dependence is not as strong as the one reported in [8], and the one shown in figure 4 [11]. This is likely due to the stronger laser intensity we have in the gas target that washes out the CEP dependence to some extent [46]. For the one-cycle gated pulses, a partial gating is achieved as expected. At certain CEP values, a continuous spectrum is generated at energy regions where the harmonic peaks can be resolved by our spectrometer (figure 7(e)), indicating the generation of isolated attosecond pulses across the whole spectral region, while at some other CEP values, low contrast harmonic peaks start to show up in the plateau, indicating the emergence of a weak secondary attosecond pulse. In the case of the two-cycle gating, very strong CEP dependence is observed across the whole spectrum, isolated attosecond pulses are only generated within a small CEP window. The big difference in the photon flux between the values of the CEP that give the highest and lowest yield is also a signature of the effectiveness of the PG. The generated broad harmonic continua could support a transform limited pulse of 13 as. The next section will be devoted to the measurement of the pulse duration.

3.2. Photoelectron streaking measurement

The measurements of the attosecond pulse duration are normally carried out using photoelectron streaking technique [47]. A replica of the attosecond pulse spectrum is detected from the kinetic energies of the generated photoelectrons assuming a flat photoionization cross section within the spectral range of the attosecond pulse. A weak few-cycle laser field—phase locked to the attosecond pulse—acts as the dressing field and perturbs the momentum of the generated photoelectrons and causes the energy distribution of the detected photoelectrons to shift up and down when the dressing field is swept across the attosecond pulse in time, forming the so called streaking pattern. Depending on the amount of chirps in the attosecond pulses, different spectral
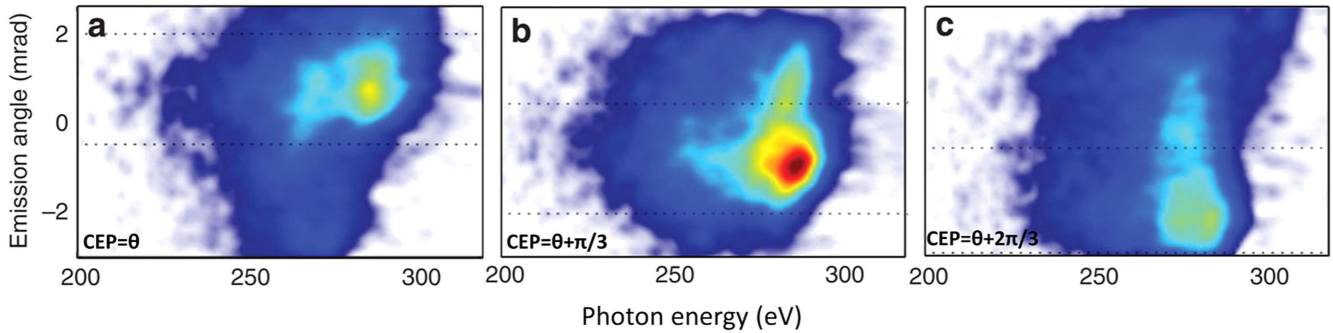
Figure 5. Isolated water window attosecond continua generated via attosecond lighthouse technique. Spectra and emission angles for three different CEP values are shown. Reproduced from [24]. CC BY 3.0.
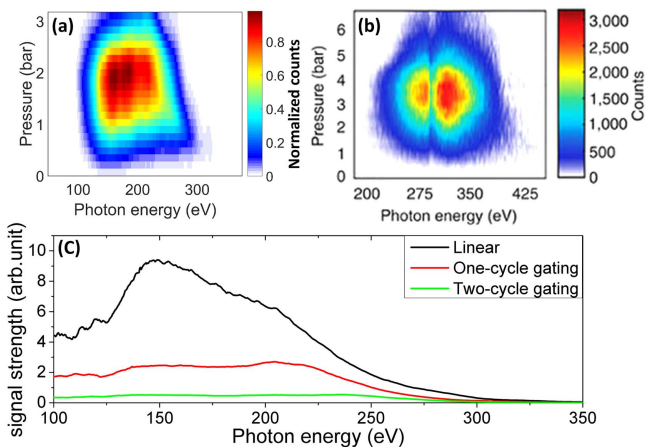

Figure 6. (a) Harmonic spectrum as a function of the neon pressure up to 3 bar, a 100 nm Sn filter is used to block the fundamental laser. Reproduced from [31]. CC BY 3.0. (b) Harmonic spectrum as a function of the neon pressure up to 6 bar, a much tighter focus is used to achieve higher cutoff, the absorption line at around 280 eV is due to carbon contamination in the chamber. Reproduced from [11]. CC BY 3.0. (c) Harmonic signal strength for linear, one-cycle gated and two-cycle gated driving fields.

components generate photoelectrons at different time and therefore experience the energy shift from the dressing field differently. By looking at the structural information in the streaking pattern, the spectral phase of the attosecond pulses can be retrieved. Employing this technique, the shortest attosecond pulse of 67 as from a Ti:sapphire laser system was successfully demonstrated [48]. Nevertheless, as already stated in the introduction, the production of photoelectrons using water window attosecond pulses driven by short/mid infrared laser systems is extremely inefficient. Therefore, no photoelectron streaking measurements covering water window have been realized until our work. Saito *et al* recently reported the first photoelectron streaking measurement using a 1.7 μm laser [45], however the photon energy is limited to within 100 eV due to the limited reflection bandwidth of the multilayer mirror. Also, very recently, Thomas *et al* reported the shortest attosecond pulse of 43 as driven by a 1.8 μm laser and characterized by photoelectron streaking measurement, however the photon energy is limited to below 180 eV [49].

Due to the difficulties in performing photoelectron streaking measurements using long wavelength drive laser,

alternative techniques have been proposed and demonstrated. Zhang *et al* developed an all optical technique to avoid the needs for photoelectrons, named photonics streaking [26]. In this technique, the far-field pattern of an isolated attosecond pulses is perturbed and modulated by a weak synchronized second harmonic field to form a photonics streaking pattern. Such photonics streaking is recorded and retrieved at each photon energy to obtain the spectral phase of each spectral component individually. The relative spectral phase is then obtained from the oscillation phase of the spatial distribution. Such technique does not provide direct access to the information of the temporal phases and is cumbersome to apply to attosecond pulses with ultra broad bandwidth.

To better characterize the attosecond pulses reach the water window, photoelectron streaking is preferred. As illustrated in figure 3, using a grazing incidence, nickel coated toroidal mirror, we focus the generated soft x-ray laser into a second gas target to generate photoelectrons from neon/helium. The photoelectrons are collected by a 3 m long magnetic bottle electron TOF spectrometer. When one- (two-) cycle gated laser pulses are used, with 100 nm Sn filter, around 1500 (200) electrons are detected per second, which is sufficient to provide enough statistics within a reasonable time frame for a streaking measurement. The photon flux is measured with an XUV photodiode (IRD AXUV100), and estimated to be around 1×10^7 and 2×10^6 photons per second over the entire bandwidth for the one-cycle and two-cycle gated cases, respectively.

The dressing field for the streaking measurement is split off the 1.7 μm laser using a 10% reflective beam splitter. This dressing arm recombines with the HHG arm using a hole mirror that transmits the generated soft x-ray beam and reflects the dressing arm. Both arms are focused together into the second gas target. The delay of the dressing arm is controlled using a piezo motor stage with a step size of about 300 as. A 532 nm CW laser is also split by the same beam splitter and co-propagates with the two arms to form an interferogram on a CCD camera (not shown), which is used to stabilize the optical path difference of the two arms by feedback control on the piezo stage [50].

Streaking measurements using neon gas as the second gas target, namely detection gas, and a 100 nm Sn filter are shown in figure 8 for the cases of one-cycle gating versus two-cycle gating. As stated before, one-cycle gating does not
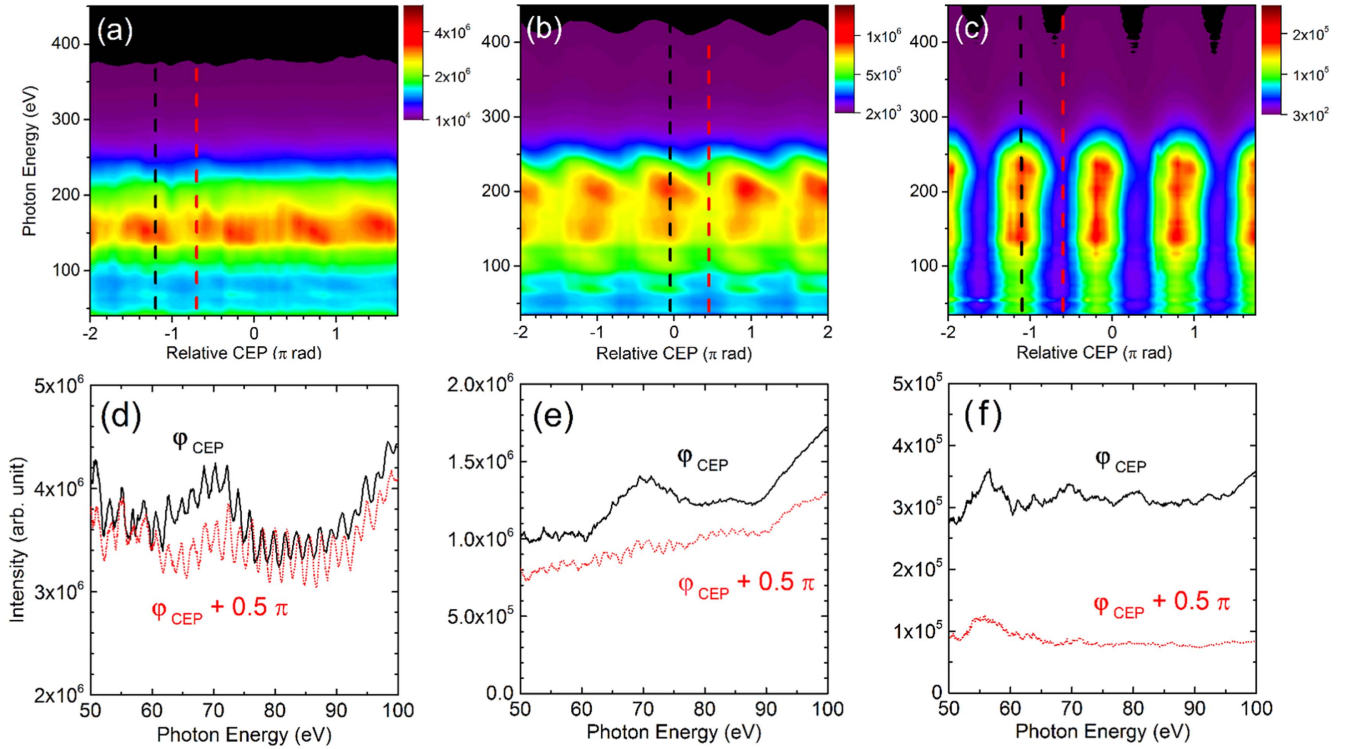
Figure 7. (a)–(c) Harmonic spectra as a function of CEP for the cases of linear, one-cycle gated and two-cycle gated driving fields, respectively. (d)–(f) Corresponding harmonic spectra line profiles at CEP values indicated by the black and red dashed lines in (a)–(c). The two CEP values are chosen to be 0.5π apart to show the CEP effect. Reprinted from [25] with the permission of AIP Publishing.

guarantee the generation of isolated attosecond pulses with our laser condition, this is clearly evidenced by the half-optical-cycle-spaced streaking peaks in figure 8(a), indicating that two attosecond pulses separated by half-optical-cycle are streaked in the opposite directions by the dressing field, forming the so-called backwards streaking. Nevertheless, a proper choice of the CEP value could eliminate such backwards streaking and provide a clean streaking measurement of isolated attosecond pulses, as indicated in figure 8(b). Figure 8(c) shows the streaking measurement with two-cycle gating, clearly indicating the generation of isolated attosecond pulses.

During the process of attosecond pulse emission, within one half-cycle of the laser electric field, electrons are pulled away from their parent ions at different phases (or time) and recombine at different phases, leading to the emission of different spectral components of the attosecond pulses. This gives rise to the intrinsic atto-chirp of the generated attosecond pulses. The ionization phase that gives the cutoff photon energy is around $17°$ according to classical calculations [51], ionization phases before and after this phase will lead to long and short trajectories, correspondingly. In experiment, we phase match the short trajectory which has a positive atto-chirp [52], meaning that low energy photons are emitted before the high energy photons. Such time difference can also be seen in figure 8(c), where the streaking peaks at high energies are lagged behind the low energy ones, as guided by the tilted line in the figure. Such tilt is a clear signature of the positive chirps in the attosecond pulses. The asymmetry of the

counts in the rising and falling edges of the streaking trace is another signature of the existence of the attochirp.

In order to compensate for the positive chirp, metallic filters or gas mediums with negative group delay dispersion (GDD) and good transmission in the vicinity of the water window are needed [29]. Sn filter is a good candidate for providing negative GDD while has a good transmission above 100 eV, as depicted in figure 9. Although the GDD starts to bend towards zero above 200 eV, indicating that the chirp above 200 eV will not be well compensated, as will be seen later. To achieve the best compression, we experiment with Sn filters of various thickness, ranging from 100 to 500 nm. With each additional 100 nm, the transmission is reduced by 40%, therefore more integration time is needed. To this end, the long term CEP stability as elaborated before is the key to the streaking measurement with thick filters.

Streaking traces with five different filter thicknesses are shown in figure 10. To better visualize the effect of increasing filter thickness, we Fourier transform the data at each slice of the photoelectron energies for all streaking traces. The DC component of the Fourier transform is filtered out and the frequency component corresponding to the driving laser frequency oscillation (LFO) is inverse Fourier transformed with its real part plotted in the middle panel of figure 10 [53]. This LFO component has twofold information. First, the oscillation peaks in the streaking traces at different photoelectron energies are directly reflected as the peaks (red blob) and valleys (blue blob) in the LFO components, namely phase angle, and the tilt of the phase angle directly reflects the amount of the chirps that are in the attosecond pulses. Second,
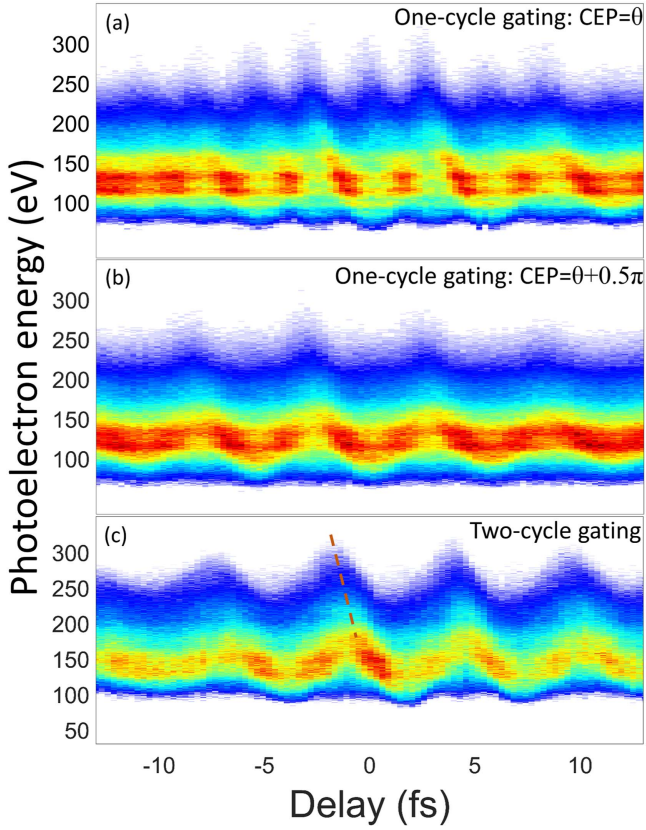
Figure 8. (a), (b) The photoelectron streaking spectrograms using one-cycle gated driving field with two different CEPs that are 0.5π apart. (c) Photoelectron streaking spectrogram using two-cycle gated driving field, the dashed line is a visual guide for the intrinsic atto-chirp.
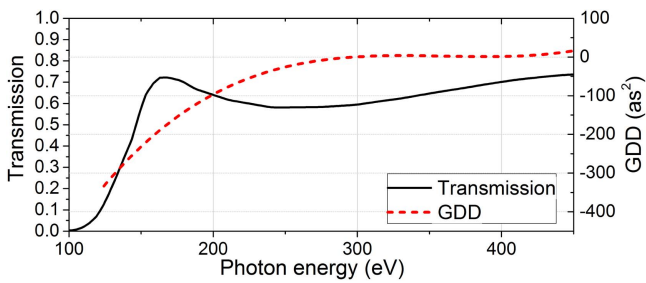

Figure 9. Transmission and group delay dispersion (GDD) curves for a 100 nm Sn filter in a photon energy range of 100–450 eV.

the asymmetry of the counts in the rising and falling edges of the streaking trace is also encoded in the LFO components, mainly in the center energy region around 150 eV. A large asymmetry, representing large chirps, will cause more signal to emerge at the center, which will disappear when no asymmetry is presented. However in our case, this signature is not easily observed due to the steepness of the spectrum in the center and the large streaking amplitudes. Nevertheless, it is easy to tell that as we add thicker filters, the tilt of the phase angle becomes less, as indicated by the dashed lines in figure 10, meaning that the chirps are compensated better. However, the tilt above 225 eV remains, which agrees well with the GDD curve of the Sn filter.

So far, all the streaking measurements are performed using neon as the detection gas. When a broadband water window attosecond pulse photoionizes neon atoms, photoelectrons from both the 2p and 2s electronic orbitals will be generated. The photoionization cross section from these two orbitals in our photon energy range differs only by about a factor of two [54], as indicated in figure 11, and the generated photoelectron energies are about 30 eV apart. Therefore, our broad photoelectron spectrum spanning from 100 eV to above 250 eV inevitably contains contributions from both orbitals. Moreover, previous studies suggest that photoionization from these two orbitals has a small time delay on the order of a few tens of attoseconds [55], which will complicate the interpretation of the measurements. To avoid multi-orbital contribution, helium gas is needed as the detection gas at the cost of a further reduction on photoionization cross section [56], see figure 11. A streaking measurement using helium as detection gas and with 400 nm Sn filter is shown in figure 12(A). Only the range of slightly over two optical cycles is covered due to the extremely low photoelectron counts of around 10 electrons per second.

Now we have the streaking measurements and can qualitatively determine the compensation of the atto-chirp, next section will focus on the retrieval of those attosecond pulses quantitatively.

4. Attosecond pulse retrieval

Under the strong field approximation, the streaked spectrogram can be expressed as,

$$S(p, \tau) = |\int dt E(t - \tau) d(p + A(t)) e^{-i\phi(p,t)} e^{i(p^2/2 + I_p)t}|^2, \tag{1}$$

where $E(t)$ is the electric field of the attosecond pulse to be retrieved, p is the momentum of the generated photoelectrons, τ is the delay between the attosecond pulse and dressing pulse, d is dipole transition matrix element representing the transition from the ground state to the continuum, $A(t)$ is the vector potential of the dressing field, I_p is the ionization potential of the detection gas atom, and $\phi(p, t)$ can be written as,

$$\phi(p, t) = \int_t^{\infty} dt'[pA(t') + A^2(t')/2]. \tag{2}$$

The expression of $S(p, \tau)$ reads very similar to the definition of a FROG spectrogram, which is expressed as,

$$S_{FROG}(\omega, \tau) = |\int dt P(t - \tau) G(t) e^{i\omega t}|^2, \tag{3}$$

with the pulse function $P(t - \tau)$ corresponding to the term of $E(t - \tau) d(p + A(t))$ and the gate function $G(t)$ corresponding to $e^{-i\phi(p,t)}$. Then the retrieval of the attosecond pulse can be mimicked as the retrieval of the pulse function in a FROG retrieval problem, which is well developed and widely studied. This is the so called FROG-CRAB (complete reconstruction of attosecond bursts) method [57] and is widely used to retrieve attosecond pulse durations, facilitated
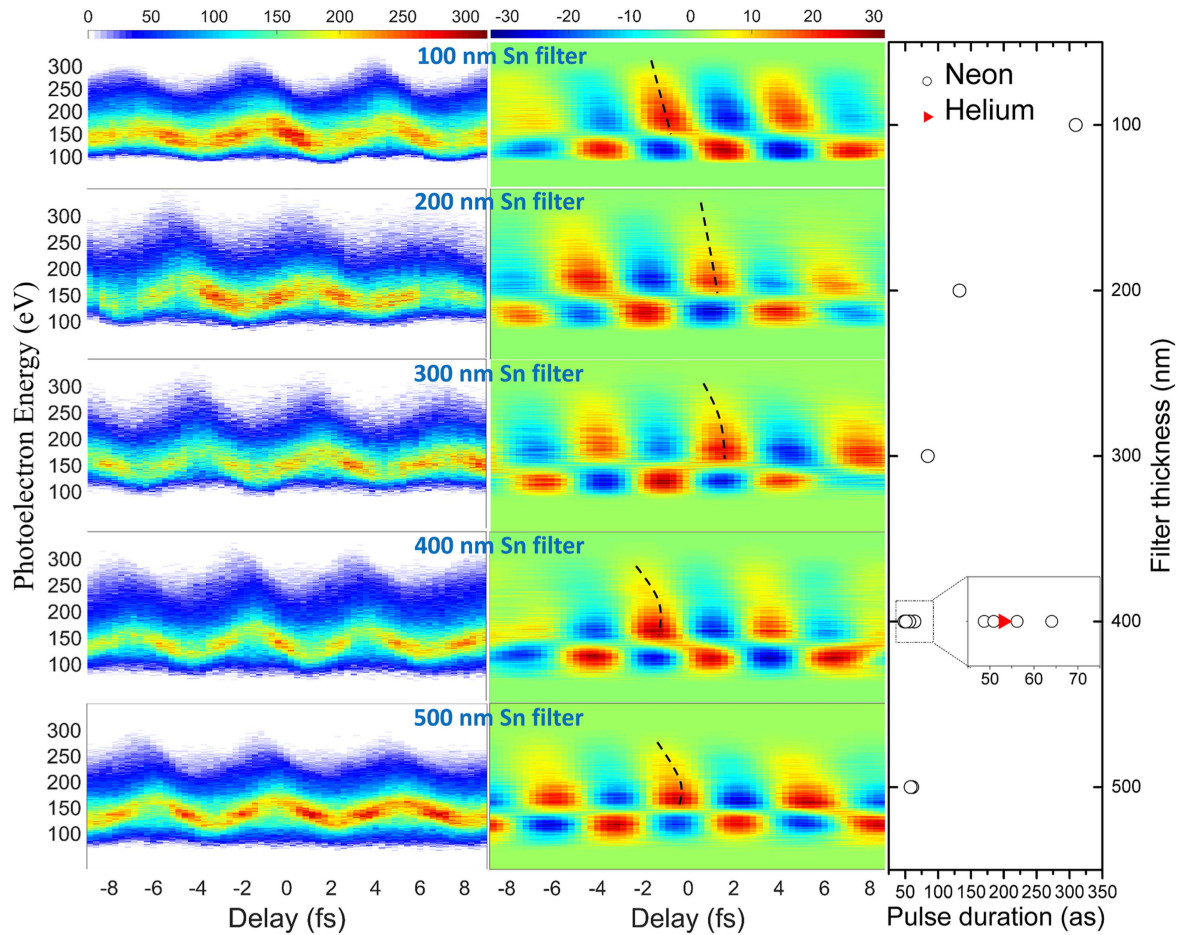
Figure 10. Left panel: streaking spectrograms with atto-chirp compensation using 100 nm to 500 nm Sn filters with an interval of 100 nm. Middle panel: corresponding traces for the S_ω at the driving LFO. The dashed lines are visual guides for the effect of the atto-chirp compensation. Right panel: corresponding retrieved pulse durations, black circles are results from using neon as the detection gas, red triangle is the result from using helium as the detection gas.
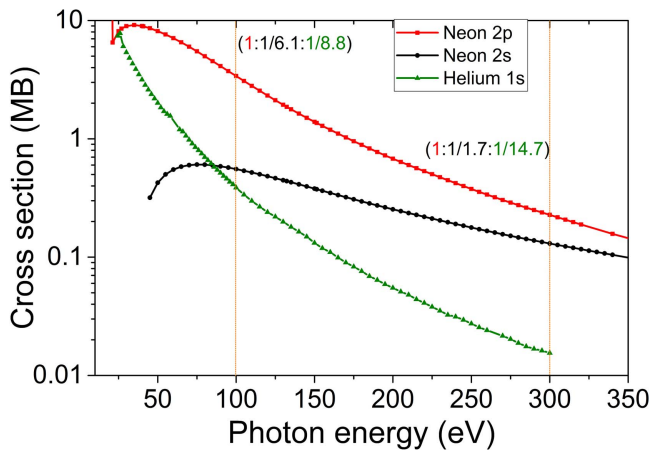

Figure 11. Photoionization cross section from neon 2p, neon 2s and helium 1s orbitals in the experimental photon energy range. At 100 eV, ratio of the cross section from these three orbitals is 1:1/6.1:1/8.8, at 300 eV, such ratio becomes 1:1/1.7:1/14.7.

by retrieval algorithms such as principle component generalized projection algorithm [58], least squares generalized projection algorithm [59] and ptychographic reconstruction technique [60]. However, in order to apply these techniques, a strong assumption needs to be enforced. In the FROG equation, both the pulse and gate functions are only functions of time, while the corresponding terms in the streaking equation have both time and momentum dependence. Therefore, in FROG-CRAB, p is substituted with its central momentum p_0 to remove the momentum dependence. This is the central momentum approximation (CMA) and is only valid for narrow band attosecond pulses, meaning that the ratio of the bandwidth of the pulse and the central photon energy is much smaller than 1. In our case, this ratio is very close to 1, obviously violating the CMA, making the FROG-CRAB technique unapplicable.

New techniques have been developed to accommodate the emerging attosecond sources with broader and broader bandwidth. Keathley *et al* recently proposed a technique named Volkov transform generalized projection algorithm that does not require Fourier transform and only apply least squared minimization algorithm in the frequency domain, therefore circumvents the needs for CMA [61]. Very recently, Zhao *et al* also proposed a phase retrieval algorithm that does not require CMA and is applicable to broadband soft x-ray attosecond pulses [62]. This technique expands the unknowns—phase of the attosecond pulse and IR field—in terms of B
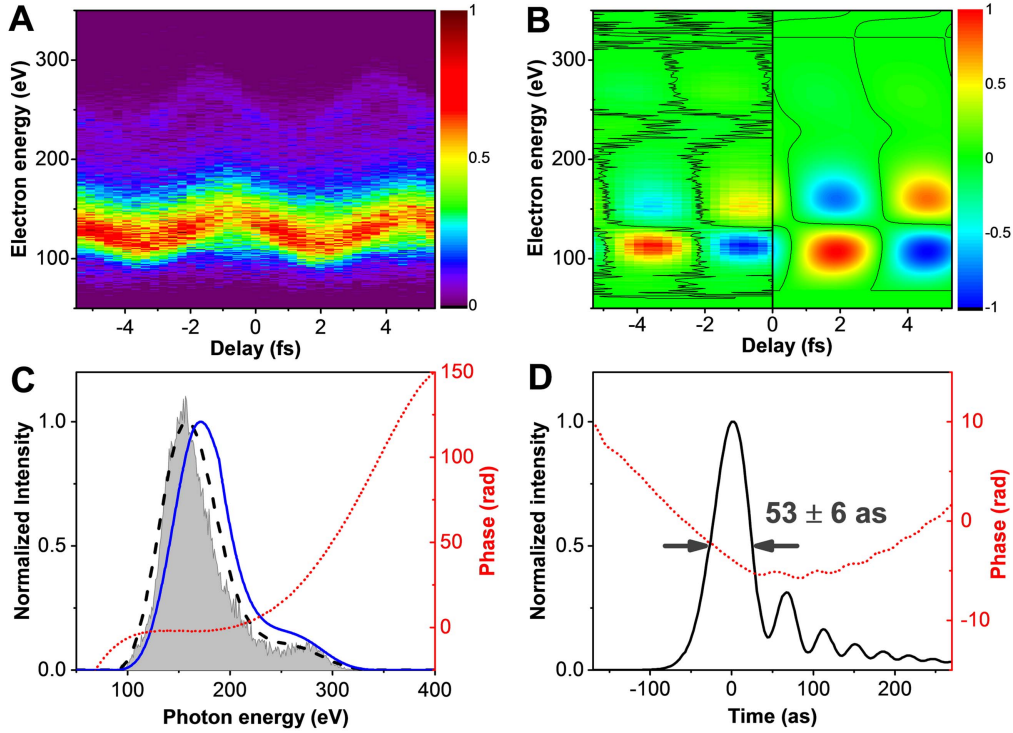
Figure 12. (A) Photoelectron streaking spectrogram with a 400 nm Sn filter and using helium as detection gas. (B) Experimental (-5 to 0 fs) and retrieved (0 to 5 fs) S_ω traces from the spectrogram. (C) Measured (gray shaded area), retrieved (black dashed line) and dipole phase corrected (blue solid line) spectra and retrieved spectral phase (red dotted line). (D) Retrieved temporal intensity profile (black solid line) and temporal phase (red dotted line) of the 53 as pulse. Reproduced from [31].

spline functions and uses genetic algorithm to retrieve the coefficients of the B spline functions and therefore retrieves the phase of the attosecond pulse. However, both techniques have not been extensively tested yet. Our group demonstrated a technique in 2010 that was intended for ultra-broadband attosecond pulse characterization, namely phase retrieval by omega oscillation filtering (PROOF) [53]. In this technique, the need for CMA is circumvented by using alternative procedures that tracks phase angle and modulation depth of the streaking traces that oscillates at the dressing field frequency, as shown in the middle panel of figure 10. Such technique has been successfully applied to retrieve a 67 as XUV pulse that covers over 30 eV bandwidth at around 60 eV. Although, the dressing field intensity needs to be low enough to avoid multiphoton coupling when PROOF is implemented.

To retrieve the pulse duration of our broadband soft x-ray attosecond pulses reach the water window, we apply the PROOF technique while keeping the driving field intensity to a level of $10^{11}\,\mathrm{W\,cm^{-2}}$. In PROOF, the photoelectron streaking spectrogram is broken down into its primary Fourier components,

$$S(p, \tau) = S_o(p) + S_\omega(p, \tau) + S_{2\omega}(p, \tau), \qquad (4)$$

where S_o is the DC component that does not change with delay, S_ω and $S_{2\omega}$ oscillate with the dressing laser frequency and twice the frequency, respectively. The information of the attosecond pulse duration is encoded in the term of S_ω, which can be expressed as,

$$S_\omega(p, \tau) = \gamma(p)\sin(\omega\tau + \alpha(p)), \qquad (5)$$

with $\gamma(p)$ and $\alpha(p)$ being the modulation depth and phase angle as mentioned before in section 3.2. The measured counterpart of S_ω is displayed in the middle panel of figure 10. Then the goal of the iterative algorithm used in PROOF is to minimize the error between the measured $S_\omega(p, \tau)$ and the calculated one assuming the spectral amplitude and phase of the attosecond pulses. In the algorithm, the error between the experimental and guessed $\gamma(p)$ and $\alpha(p)$ are separately minimized, in an iterative fashion. The algorithm proceeds as follows:

Initialization: Let the spectral amplitude of the attosecond photoelectron burst be given by $I(p) = \frac{S_o(p)}{2}$. This is a very accurate guess in the case where the streaking intensity is low; however, it must be refined by further iteration (spectrum optimization) under practical experimental conditions. To avoid introducing noise into the algorithm, the spectrum is smoothed using a cubic spline fitting function.

Phase optimization: Guess the spectral phase of the attosecond burst $\phi(p)$ which minimizes the error function between the experimentally-obtained phase angle $\alpha(p)$ and that calculated from the guessed $I(p)$ and $\phi(p)$. For this minimization, the value of the phase at each electron energy is allowed to vary between 0 and 2π, and the spectral phase function $\phi(p)$ is obtained by unwrapping the phase and applying a cubic spline fitting before evaluating the error function, in order to avoid introducing noise into the algorithm.

Spectrum optimization: Guess the spectral amplitude of the attosecond burst $I(p)$ which minimizes the error function
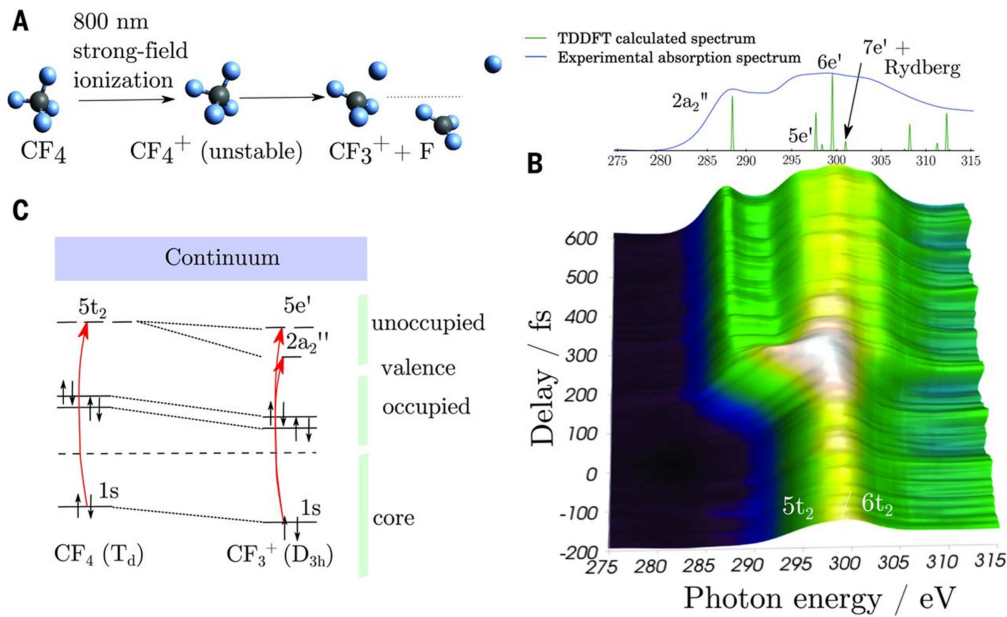
Figure 13. Water window transient absorption experiment following the dissociation dynamics of CF_4 molecule after strong-field ionizaton. (A) A cartoon of the dissociation path. (B) The absorbance as a function of the pump probe laser delay. In this case, pump is an intense 800 nm laser pulse and probe is the water window high harmonics. (C) The transition orbital paths for CF_4 and CF_3^+. From [15]. Reprinted with permission from AAAS.

between the experimentally-obtained modulation amplitude $\gamma(p)$ and that calculated using the guessed $I(p)$ and $\gamma(p)$. For this minimization, the value of the amplitude is allowed to vary freely, and the spectral amplitude function $I(p)$ is obtained by applying a cubic spline fitting before evaluating the error function, in order to avoid introducing noise into the algorithm.

Repeat phase and spectrum optimization iteratively. After each iteration, evaluate the error function between the experimentally obtained laser-frequency filtered spectrogram $S_\omega(p, \tau)$ and that calculated using the guessed $I(p)$ and $\phi(p)$. Once the error has decreased to a suitable value, stop the loop and export the guessed $I(p)$ and $\phi(p)$. Apply the dipole correction to the guessed $I(p)$ and $\phi(p)$ to obtain the attosecond photon pulse spectrum and phase.

The metrics used to evaluate the accuracy of the retrieval are therefore the agreement between the filtered spectrogram $S_\omega(p, \tau)$ and that calculated from the guessed $I(p)$ and $\phi(p)$, as well as the agreement between the measured and guessed photoelectron spectrum. The measured and retrieved $S_\omega(p, \tau)$ are shown in figure 12(B) for the streaking measurement with a 400 nm Sn filter and helium as the detection gas. The agreement is excellent, with the only discrepancy occurring in the photoelectron spectral region around 225 eV, where the experimental modulation amplitude drops to nearly zero, and the phase angle cannot be accurately extracted. The measured and retrieved spectra also show good agreement as depicted in figure 12(C), the retrieved spectral phase exhibits a parabolic phase above 200 eV, which agrees with the GDD curve of the Sn filter (figure 9(b)). The retrieved pulse duration lands at

53 as, which is the shortest laser pulse ever characterized covering the water window spectral region.

To further support our retrieved results, we retrieve pulse durations for the results displayed in the left panel of figure 10. The retrieved pulse duration as a function of the Sn filter thickness is shown in the right panel of figure 10. As is clearly evident, adding more and more filters results in a continuous reduction in attosecond pulse duration below 400 nm, beyond which the chirp of the attosecond pulse is over-compensated and the pulse duration goes up again. With a 400 nm Sn filter, multiple measurements and retrievals are carried out to further validate the repeatability of our result, as presented in the inset of the right panel in figure 10. The standard deviation of the five measurements and retrievals at 400 nm Sn filter is calculated to be 6 as, and is used as the error bar for the 53 as pulse (figure 12(D)). The photon flux of this 53 as pulse is estimated to be around 5×10^5 photons per laser shot for the entire bandwidth, and the portion above the carbon K-edge is 1×10^4 photons per laser shot.

5. Attosecond transient absorption (ATA) in the water window

As elaborated in the introduction, one of the most important goals of developing these water window attosecond sources is to probe sub-femtosecond electron dynamics happening in organic molecules, such as charge migration and core hole dynamics [63], which are important initial steps that lead to subsequent chemical reactions. State-of-art techniques such as ATA are successfully demonstrated to be able to resolve
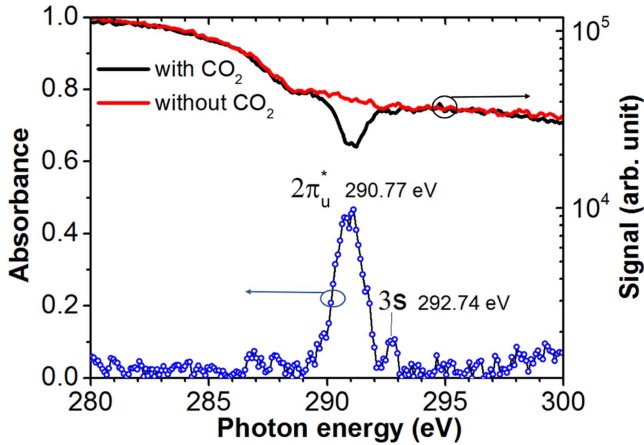
Figure 14. Blue curve and circles show the absorbance from carbon dioxide molecules. The two absorption peaks correspond to $C_{1s} \rightarrow 2\pi_u^*$ and $C_{1s} \rightarrow$ Rydberg 3s state. Carbon dioxide gas with 25 Torr mm pressure-length product is used in the measurement. Red and black curves show the harmonic spectra with and without CO_2 gas in the gas cell.

sub-cycle electron dynamics such as AC stark shift, Ponderomotive energy shift, Autler–Townes splitting [64] and auto-ionization dynamics of Rydberg states [65], although the photon energy range is currently limited to within 100 eV. Very recently, Pertot *et al* [15] and Attar *et al* [16] both reported transient absorption experiments at the carbon K-edge, revealing molecular structural deformation processes that both happen in a 40–100 fs time scale. Figure 13 shows the result obtained in [15]. Upon removing one valence electron from CF_4 molecule, CF_4^+ ion is unstable and will dissociate and deform to CF_3^+ ion plus a fluoride atom. The absorption lines near the carbon K-edge are substantially different for the CF_4 molecule and the CF_3^+ ion, see figure 13(C). Therefore, by tracking the time resolved near edge absorption features, a 40 fs time frame can be assigned to this chemical reaction path.

However, up to now, sub-femtosecond dynamics near the carbon K-edge and beyond have been out of reach, either due to the relatively long soft x-ray pulses or its low photon flux. The attosecond sources we have developed could be an ideal source for ATA experiments in the water window revealing sub-femtosecond dynamics in carbon containing targets.

To demonstrate the feasibility of conducting such experiment, a carbon K-edge absorption measurement is performed and the result is shown in figure 14. For this demonstration, the second gas jet in figure 3 is replaced with a 1 mm long gas cell filled with 25 Torr carbon dioxide. A 2400 lines mm^{-1} soft x-ray grating and an x-ray CCD camera are used substituting MCP/phosphor pairs to achieve high spectral resolution near the carbon K-edge. Figure 14 shows the absorption spectrum after 4 min integration time. The absorbance is extracted as $A(\omega) = \ln[S_{in}(\omega)/S_{out}(\omega)]$, where $S_{in}(\omega)$ and $S_{out}(\omega)$ are the input and output spectra (red and black curves in figure 14) of the absorption cell, respectively. The main absorption peak at 290.77 eV corresponds to the promotion of a carbon 1s electron to the lowest unoccupied molecular orbital $2\pi_u^*$, while the satellite peak at 292.74 eV corresponds to the transition to the Rydberg 3s orbital [66]. It

is clear that our water window attosecond sources can easily access these absorption features that will allow us to trace the temporal evolution of π- or σ-bonding electrons in biomolecules. Such experiment is undergoing and will be reported in the near future.

6. Push the photon energy to even higher—design of high energy few-cycle mid-infrared driving lasers

The attosecond source we developed only contains a small portion of photon energy in the water window. As discussed in the introduction and illustrated in table 1, in order to push the attosecond photon energy further into the water window, high energy few-cycle mid-infrared driving lasers are demanded. In this section, we will briefly overview the current research status on development of such mid-infrared lasers that extend wavelength around 3 μm and beyond.

6.1. High-energy two-cycle pulses around 3 μm

The generation of low-energy few-cycle pulses or broad bandwidths needed for supporting few-cycle pulses near 3 μm has been reported by employing OPA technique [67–69]. However, upscaling to mJ level in those systems seems challenging. For example, 45 fs pulses at 3 μm were achieved by OPA in $KNbO_3$ [67], but $KNbO_3$ crystal has multi-domain issues; 3–5 μm spectra supporting three-cycle pulses were achieved by OPA in $LiIO_3$ [68], but the damage threshold of $LiIO_3$ is rather low; 25 fs pulses at 3.5 μm were achieved by OPA in PPSLT [69], but the size and thickness of PPSLT are limited. Meanwhile, the generation of high-energy 3 μm pulses has been reported utilizing OPCPA technique [70–73]. For example, 13.3 mJ pulses with center wavelength between 3.3 and 3.95 μm [72] have been generated via OPCPA in $LiNbO_3$ crystal, and 8 mJ pulses at 3.9 μm [73] have been achieved via OPCPA in KTA crystal. However, the pulse durations in those two systems have been limited to multi-cycles with 111 fs and 83 fs, respectively. This is due to the limited parametric bandwidth of $LiNbO_3$ and KTA in the OPCPA process. Thus, it has been a challenging task to generate high-energy few-cycle pulses around 3 μm primarily due to the limited choice of large-size nonlinear crystals in OPA and limited gain bandwidths in OPCPA.

One approach for generating high-energy few-cycle pulses around 3 μm is by using broadband-pumped dual-chirped OPA (DC-OPA). DC-OPA is essentially an OPCPA pumped by chirped broadband pulses [75–80]. Thus, OPCPA system described in section 2 can also be treated as a DC-OPA. It was found that a broadband Ti:sapphire pump and a broadband seed (2.4–4.0 μm) can phase match very well in a MgO:LiNbO$_3$ DC-OPA in the temporal domain if chirps are managed properly. Unlike the common few-cycle OPCPA and DC-OPA, this broadband-pumped DC-OPA allows the use of longer crystals without either gain narrowing or efficiency loss since phase matching occurs between the individual temporal slice of pump spectrum and that of seed spectrum, which is illustrated by the phase matching curve in
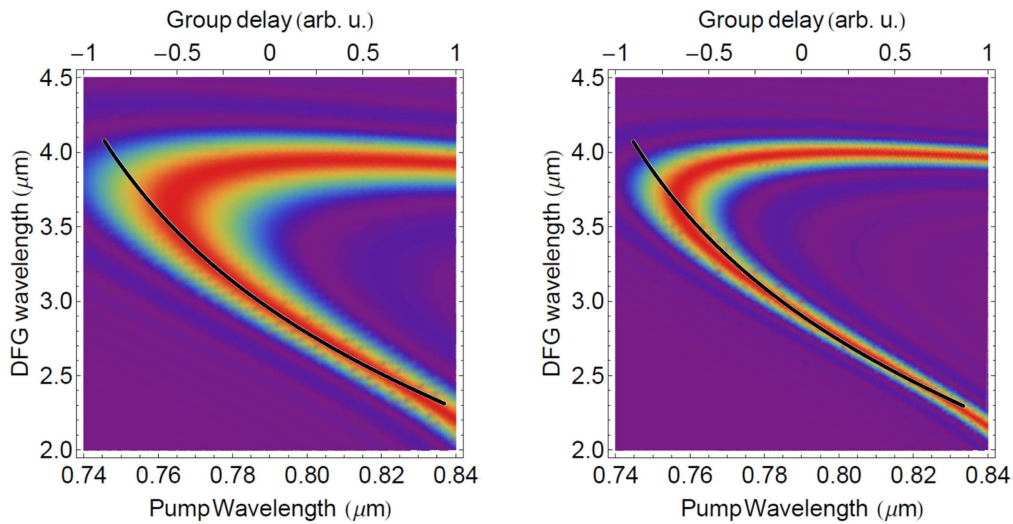
Figure 15. The calculated phase-matching efficiency as a function of pump and idler wavelengths for a noncollinear configuration (PM angle $\theta = 44.4°$, noncollinear angle $\alpha = 0.5°$). The black line represents the chirped signal pulse with its corresponding wavelengths marked by the left axis and its temporal chirp marked by the top axis. Left: 2 mm MgO:LiNbO$_3$; right: 4 mm MgO:LiNbO$_3$. Reproduced with permission from [74].
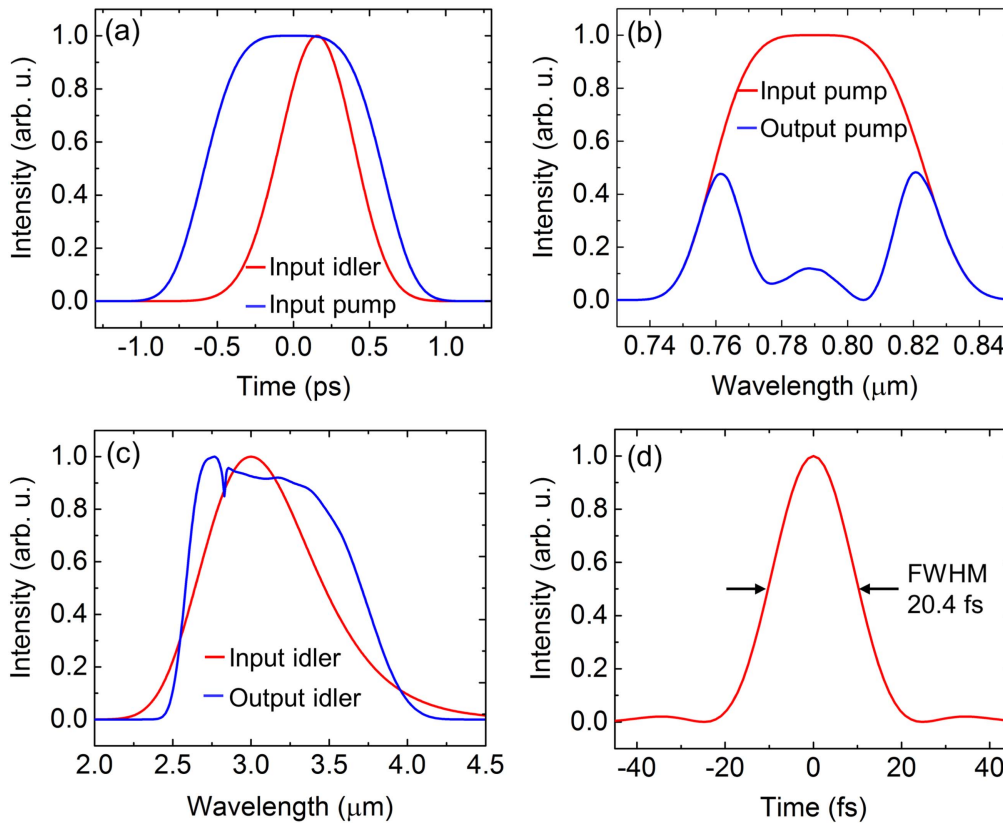

Figure 16. Simulation results of the broadband-pumped DC-OPA in a 2.4 mm MgO:LiNbO$_3$. Reproduced with permission from [74].

figure 15 and has been confirmed by simulations in [74]. The approach for generating and compressing such a two-cycle pulse at 3.2 μm is very similar to figure 1(c) except for the crystal for seed generation and material for compression. The broadband seed can be generated by DFG in either BIBO or KTA [81], and the compression can be done in bulk silicon to compress the pulse in the 2.4–4.0 μm spectral region. An example for simulation results is shown in figure 16,

indicating that a mJ-level two-cycle pulse at 3.2 μm can be generated in MgO:LiNbO$_3$ considering a 19% calculated conversion efficiency [74] with more than 5 mJ pump energy. This broadband-pumped DC-OPA has a great advantage over the narrowband-pumped OPCPA in term of the phase matching bandwidth, especially in the non-degenerate configuration where the phase matching bandwidth is usually narrow; it also has advantages over frequency domain OPA
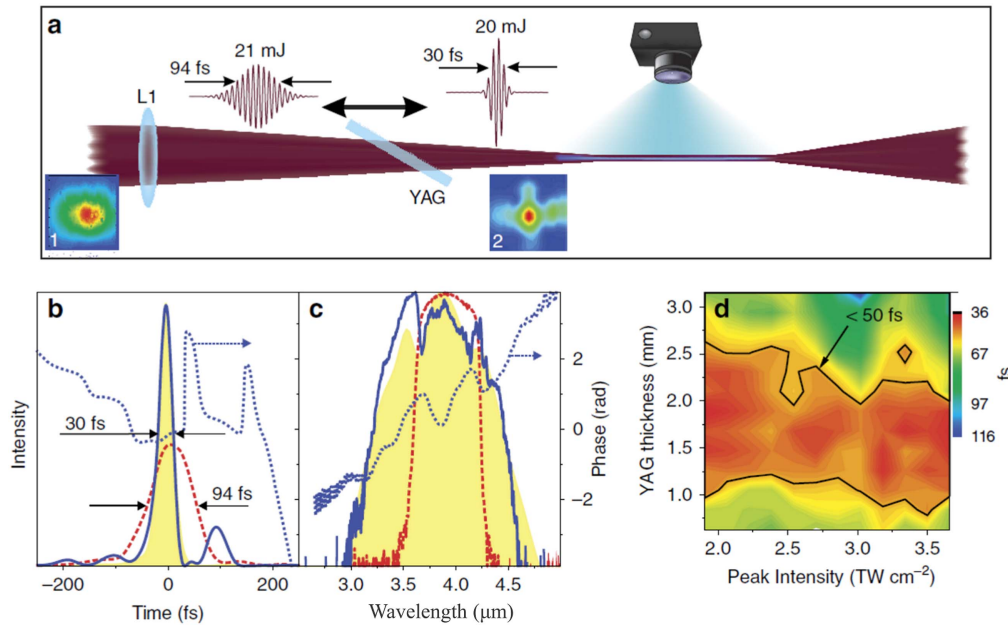
Figure 17. Setup for self-compression and characterization of mid-infrared pulses. (a) Sketch of the experimental setup: three-fold self-compression of 94 fs, 21 mJ pulses, centered at 3.9 μm, is achieved in a 2 mm thick YAG plate placed at a certain distance from the focusing lens L1; (b), (c) retrieved from SHG FROG measurements temporal (b) and spectral (c) pulse profiles of the output of 3.9 μm OPCPA system (dashed red line) and self-compressed in YAG pulses (blue solid line); the yellow area represents calculated temporal profile and spectrum of the self-compressed pulse (normalized intensity). Dotted blue lines show retrieved temporal and spectral phases; (d) 3D-map representing the dependence of the output pulse duration on the thickness of the material and on the input peak intensity. Reproduced from [83]. CC BY 3.0.

(FOPA) [82] in that it can preserve the CEP of the seed pulse and compress the pulse in a bulk material almost without loss of pulse energy, since FOPA tends to deteriorate the CEP of the seed pulse if without an active feedback, as well as results in loss of pulse energy because of compression using gratings. This DC-OPA design can also be applied to the $KNbO_3$ nonlinear cyrstal, which has a higher nonlinearity and damage threshold. The problem is that high-quanlity $KNbO_3$ can be hardly bought.

Another approach for generating high-energy few-cycle pulses around 3 μm is by nonlinear compression of multi-cycle pulses in bulk materials utilizing the interplay between anomalous dispersion and SPM [83]. The experimental results from [83] are shown in figure 17. The sub-100 fs, 21 mJ pulses centered at 3.9 μm were generated from a hybrid OPA/OPCPA system. The broadened spectrum due to SPM is self-compressed from 94 to 30 fs, which is a three-cycle pulse at 3.9 μm and very close to the transform-limited pulse width of 26 fs. The energy of the compression exceeds 19.7 mJ with a compression efficiency of over 93%. This approach is a good alternative to achieve few-cycle pulses in the mid-infrared region where gain spectrum in OPCPA/CPA is not broad enough.

6.2. Towards terawatt sub-cycle long-wave infrared pulses

Rapid progress has been made on the generation of mid-IR laser sources around 5 μm [84–87] and 7 μm [87] via OPA or OPCPA in ZGP crystals pumped around 2 μm. Recently, mJ level femtosecond OPCPA source around 5 μm operating at kilohertz repetition rates has been developed [88]. As shown in figure 18, the OPCPA is seeded by a compact fiber based front-end and is pumped by a 2 m Ho:YLF laser based on CPA. The seed pulse is generated at 3.4 μm covering 700 nm FWHM bandwidth through DFG between the 1 and 1.5 μm pulses in a periodically poled lithium niobate crystal (MgO: PPLN). The 2 μm pump can provide an energy as high as 25 mJ with an almost transform-limited pulse duration of 4.3 ps. After three-stage OPCPA, the 1.3 mJ idler at a center wavelength of 5.1 μm were achieved with a pulse duration of 160 fs. Further compression using a spatial light modulator (SLM) yielded a sub-five-cycle 75 fs pulse duration (figures 18(b) and (c)) with 0.65 mJ pulse energy.

Even though OPCPA bandwidth in ZGP can support few-cycle pulses near or above 5 μm, such few-cycle pulses have not been enabled partially due to the limited seed bandwidth of the signal. Another challenge comes from compression of such huge parametric bandwidth directly, in which case both AOPDF and SLM both exhibit limitations. Thus, the key to achieving few-cycle pulses around 5 μm and above is to develop broadband seed pulses and compression scheme that can control high-order phases. In [35], a design was presented which is capable of not only generating mJ-level, CEP-stable 4–12 μm pulses through DC-OPA in ZGP nonlinear crystals, but also compressing such pulses to sub-cycle duration through indirect pulse shaping. The principle is illustrated in figure 19(b), which shows that the chirp of idler can be tuned indirectly by changing the chirp of the signal and pump. The signal pulse covering 1.8–4.2 μm can be generated by DFG in a BIBO crystal [81] and the 2 μm pump can be amplified in a Ho:YLF laser. The 4–12 μm optical parametric bandwidth is achieved by tailoring the phase matching of
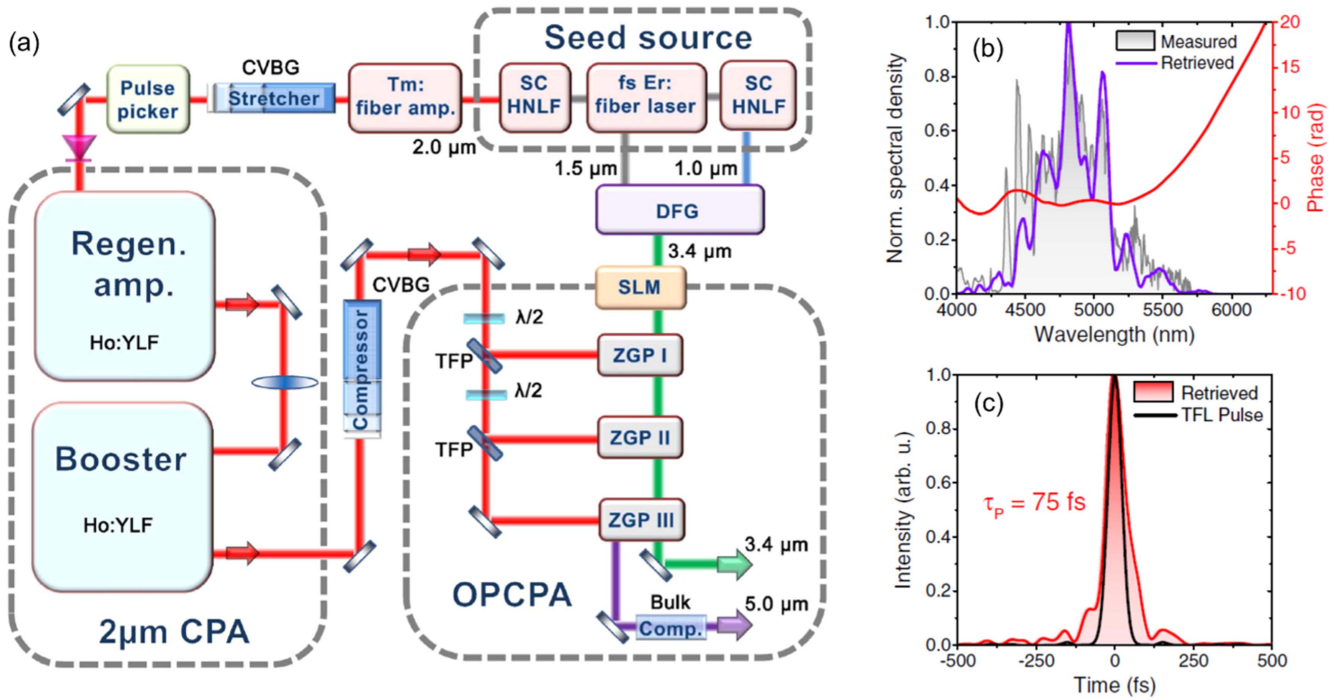
Figure 18. (a) Setup of the mid-IR OPCPA source pumped at 2 μm. The main parts are the seed source, the 2 μm Ho:YLF CPA amplifiers, DFG, the SLM, and the three OPA stages based on ZGP crystals. Regen. amp., regenerative amplifier; Booster, power amplifier; CVBG, chirped volume Bragg grating; SC, supercontinuum generation; HNLF, highly nonlinear fiber; TFP, thin-film polarizer. SHG-FROG characterization of the 5 μm OPCPA pulses: (b) optical spectrum, measured (gray), retrieved (purple) and phase (red); (c) retrieved temporal pulse shape. TFL, Fourier-transformlimited. Reproduced with permission from [88].
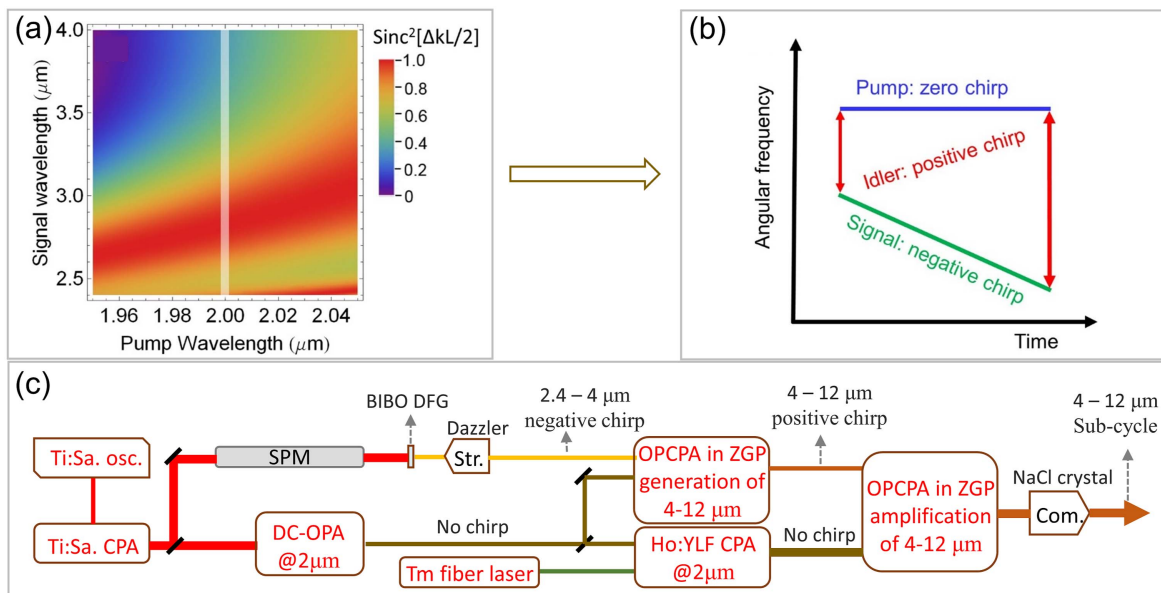

Figure 19. (a) The calculated phase matching efficiency (Sinc^2[$\Delta kL/2$]) as a function of pump and signal wavelengths for a 0.6 mm Type I (phase matching angle: 54°) ZGP crystal. Δk is the propagation constant difference and L is the ZGP crystal length. The white shaded line qualitatively shows the utilized phase matching region in the 4–12 μm OPCPA. (b) Chirp relationship among the pump, signal, and idler. (c) Proof-of-principle schematic setup for amplifying 4–12 μm idler pulses by OPCPA in a 0.7 mm ZGP pumped by a 2 μm Ho:YLF laser. Reproduced from [35]. CC BY 3.0.

ZGP shown in figure 19. The second-order phase of high-energy 4–12 μm pulses can be compensated by using NaCl crystal, which has a very small n_2 and a high damage threshold; the higher-order phase can be compensated indirectly by controlling the signal phase with a commercially available AOPDF. The simulation results for generating 4–12 μm pulses are shown in figure 20. This 4–12 μm broad pulse can be amplified to TW level pumped by either a Ho:YLF laser at 2 μm or preferably by a Cr^{2+}:ZnSe laser at 2.4 μm.
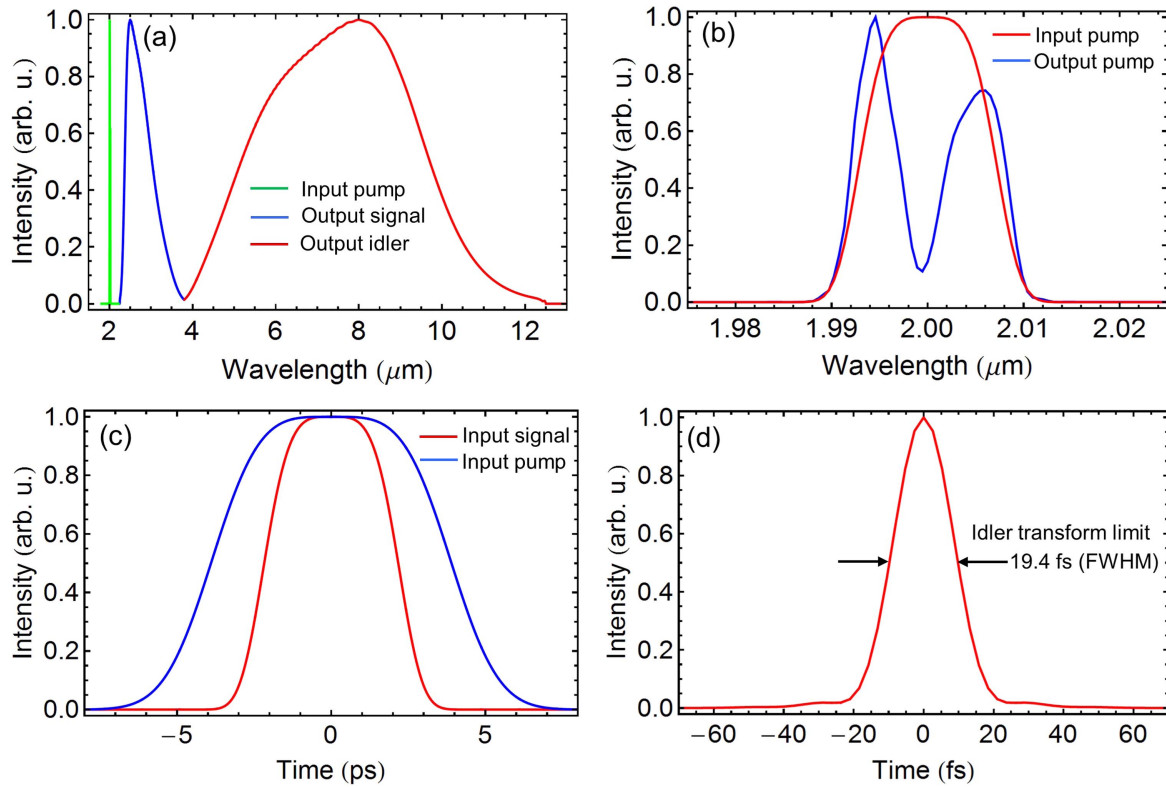
Figure 20. Simulation results for generating 4–12 μm idler pulses in a 0.4 mm ZGP OPCPA pumped by a 2 μm narrowband laser. Reproduced from [35]. CC BY 3.0.

7. Conclusion and outlook

In this paper, we reviewed recent progresses in generating attosecond continua into the water window region. In order to achieve such continua, driving lasers with few-optical-cycle in the short to mid-infrared spectral range are necessary, and these state-of-art laser systems are typically enabled by OPA followed by hollow-core fiber compression, OPCPA or DC-OPA. Although several groups have reported generation of isolated attosecond pulses covering the water window, their pulse duration measurements have not been realized until our work. There are three importance factors in our work that are essential for characterizing attosecond pulses in the water window: (1) a multi-mJ laser system at 1 kHz with two-optical cycles and exceptional long term CEP stability. (2) An efficient generation and characterization apparatus consisting of high pressure gas target for generation and magnetic bottle TOF for characterization through photoelectron streaking. (3) A retrieval algorithm that can retrieve pulse duration of broadband attosecond pulses. We have given detailed description on each factors and introduced the first photo-electron streaking measurement of broadband isolated atto-second pulses reach the water window. By carefully investigating atto-chirp compensation using Sn filters, we demonstrated a 53 as x-ray source covering water window when a 400 nm Sn filter is used under our experimental conditions.

Further scaling up the photon energy as well as short-ening the pulse duration require even longer-wavelength
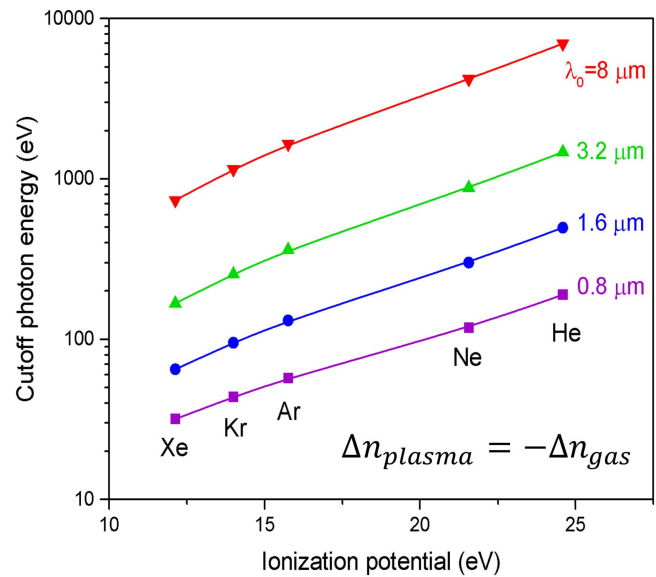

Figure 21. Calculated phase matched cutoff of high harmonic generation from various inert gases driven by lasers at different wavelengths.

driving lasers with even higher pulse energies to make up for the reduced yield due to wavelength scaling. We reviewed recent advances in producing mid- and long wave infrared lasers and briefly discussed our designs of energetic mid-infrared laser systems covering 2–4 μm and 4–12 μm. These laser sources will enable attosecond pulses covering the entire water window and even into the keV region. Figure 21 shows
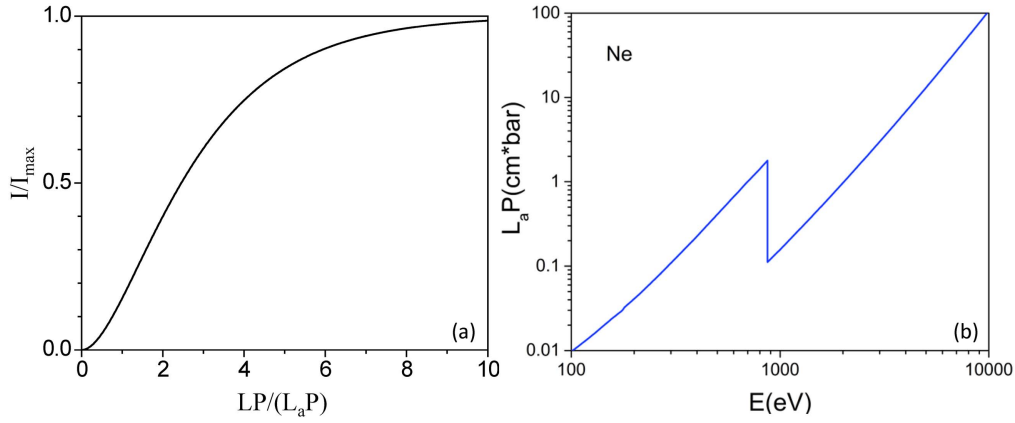
Figure 22. (a) Dependence of x-ray intensity (normalized to the maximum intensity) on the ratio between LP and L_aP.(b) L_aP of neon gas.

the expected HHG cutoff from different driving laser wavelengths under perfect phase matching condition, meaning that the plasma induced index of refraction and that of the neutral target gas is well balanced [89]. It is clear that future of the attosecond science in the water window and multi-keV region relies on the development of energetic high repetition rate laser sources at 3 μm and beyond. However, the biggest challenge is to generate these x-ray pulses with sufficient flux for applications. Once perfect phase matching is realized for a driving laser with a particular center wavelength, the maximum intensity of the x-rays with frequency, ω_X, is determined by the driving laser field strength, the single atom response, $d(\omega_X)$, and the absorption cross section of the gas, $\sigma(\omega_X)$, assuming that the length-pressure-product of the gas media LP is much larger than the absorption length-pressure-product L_aP. The upper limit of x-ray intensity at the exit of the gas target can be expressed as,

$$I_{\max}(\omega_X) = \frac{\omega_X^2}{8c\epsilon_o}|d(\omega_X)|^2\frac{1}{\sigma^2(\omega_X)}, \qquad (6)$$

where c is the speed of light in vacuum and ϵ_o is the electric permittivity [2]. The x-ray intensity can then be written as,

$$I(LP, \omega_X) = I_{\max}(1 + e^{-\frac{LP}{L_aP(\omega_X)}} - 2e^{-\frac{LP}{2L_aP(\omega_X)}}), \qquad (7)$$

which is shown in figure 22(a) as a function of the ratio between LP and L_aP. In experiment, one may choose a ratio at around 5. The absorption length-pressure-product of neon gas is shown in figure 22(b). For a medium length of 1 cm, which is the typical value of the Rayleigh range of mJ level mid- and long wave infrared lasers, the pressure should be on the order of 1–100 bar for 1–10 keV x-rays. Therefore, special gas target structures need to be designed to deliver high pressure gas to the laser focal point region. Pulsed gas nozzle and differential pumping may be used to reduce the gas load of the vacuum pumps. Although theoretically higher photon energy x-rays can be produced by using helium gas, it requires a gas target with a much larger length-pressure-product, which is difficult to construct experimentally. In addition, the single atom response of helium is weaker than neon.

The isolation of attosecond pulses at higher photon energies driven by mid- and long wave infrared lasers can also be done via PG. In fact, if we assume that the x-ray emission from

an elliptical field is dominated by those electron trajectories whose transverse displacement caused by the elliptical field is compensated by an initial transverse velocity when the electron tunnels out of the atomic binding potential [90], we can estimate the ellipticity dependent HHG yield as shown in figure 23. The ellipticity dependence increases with the increment of the driving laser center wavelength, which indicates that PG will work more efficiently with longer wavelength driving lasers. Applying attosecond streaking to characterize broadband water window and keV attosecond pulses faces new challenges. Multi-orbital contribution and orbital parity mix interference may occur and need to be taken into account during the spectral phase retrieval [91]. Neon atoms may still be a good candidate as the detection gas since it only has two shells, and the ionization cross section of the 1s orbital in the 1–10 keV range is much higher than that of helium. Nevertheless, high flux x-rays must be generated to assure reasonable signal to noise ratio in streaking experiments.

Moreover, as the GDD for most metallic filters start to approach zero above 300 eV, how to compensate for intrinsic atto-chirps and produce transform limited attosecond pulses will be challenging for water window attosecond pulses and beyond, even though the atto-chirp is expected to go down when longer driving lasers are used [52]. Alternative compensating routines such as using high pressure inert gases [92] or tailoring the electric field of the driving laser [93] might be useful candidates for atto-chirp compensation at high photon energies. Complementary techniques using two-color or multi-color field for enhancing harmonic yield may become useful in increasing photon flux for attosecond pulses at high photon energies. With sufficient flux and atto-chirp compensation, these water window attosecond sources will be ideal tools for studying ultrafast electron dynamics of biologically relevant molecules through time resolved near edge absorption spectroscopy.
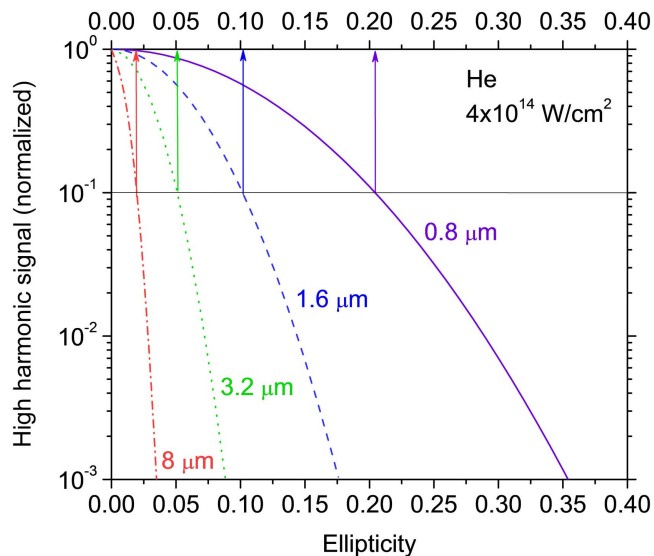
Funding

Figure 23. Ellipticity dependence of high harmonic signal for different driving laser center wavelengths. Arrows indicate the values of the threshold ellipticity for polarization gating.

ORCID iDs

Yanchun Yin ⓘ https://orcid.org/0000-0001-9034-1738
Zenghu Chang ⓘ https://orcid.org/0000-0002-0900-5911

References

[1] Krausz F and Ivanov M 2009 *Rev. Mod. Phys.* **81** 163
[2] Chang Z 2016 *Fundamentals of Attosecond Optics* (Boca Raton, FL: CRC Press)
[3] Spielmann C, Burnett N, Sartania S, Koppitsch R, Schnürer M, Kan C, Lenzner M, Wobrauschek P and Krausz F 1997 *Science* **278** 661
[4] Chang Z, Rundquist A, Wang H, Murnane M M and Kapteyn H C 1997 *Phys. Rev. Lett.* **79** 2967
[5] Popmintchev T, Chen M C, Bahabad A, Gerrity M, Sidorenko P, Cohen O, Christov I P, Murnane M M and Kapteyn H C 2009 *Proc. Natl Acad. Sci.* **106** 10516
[6] Shan B and Chang Z 2001 *Phys. Rev.* A **65** 011804
[7] Xiong H *et al* 2009 *Opt. Lett.* **34** 1747
[8] Ishii N, Kaneshima K, Kitano K, Kanai T, Watanabe S and Itatani J 2014 *Nat. Commun.* **5** 3331
[9] Takahashi E J, Kanai T, Ishikawa K L, Nabekawa Y and Midorikawa K 2008 *Phys. Rev. Lett.* **101** 253901
[10] Johnson A, Miseikis L, Wood D, Austin D, Brahms C, Jarosch S, Strüber C, Ye P and Marangos J 2016 *Struct. Dyn.* **3** 062603
[11] Teichmann S, Silva F, Cousin S, Hemmer M and Biegert J 2016 *Nat. Commun.* **7** 11493

[12] Chen M C, Arpin P, Popmintchev T, Gerrity M, Zhang B, Seaberg M, Popmintchev D, Murnane M and Kapteyn H 2010 *Phys. Rev. Lett.* **105** 173901
[13] Stein G J *et al* 2016 *J. Phys. B: At. Mol. Opt. Phys.* **49** 155601
[14] Popmintchev T *et al* 2012 *Science* **336** 1287
[15] Pertot Y *et al* 2017 *Science* **355** 264
[16] Attar A R, Bhattacherjee A, Pemmaraju C, Schnorr K, Closser K D, Prendergast D and Leone S R 2017 *Science* **356** 54
[17] Kim K T *et al* 2013 *Nat. Photon.* **7** 651
[18] Chini M, Zhao K and Chang Z 2014 *Nat. Photon.* **8** 178
[19] Goulielmakis E *et al* 2008 *Science* **320** 1614
[20] Jullien A, Pfeifer T, Abel M J, Nagel P, Bell M, Neumark D M and Leone S R 2008 *Appl. Phys.* B **93** 433
[21] Corkum P, Burnett N and Ivanov M Y 1994 *Opt. Lett.* **19** 1870
[22] Sola I *et al* 2006 *Nat. Phys.* **2** 319
[23] Mashiko H, Gilbertson S, Li C, Khan S D, Shakya M M, Moon E and Chang Z 2008 *Phys. Rev. Lett.* **100** 103906
[24] Silva F, Teichmann S M, Cousin S L, Hemmer M and Biegert J 2015 *Nat. Commun.* **6** 6611
[25] Li J, Ren X, Yin Y, Cheng Y, Cunningham E, Wu Y and Chang Z 2016 *Appl. Phys. Lett.* **108** 231102
[26] Zhang C, Brown G G, Kim K T, Villeneuve D and Corkum P 2016 *Sci. Rep.* **6** 26771
[27] Shiner A, Trallero-Herrero C, Kajumba N, Bandulet H C, Comtois D, Légaré F, Giguère M, Kieffer J, Corkum P and Villeneuve D 2009 *Phys. Rev. Lett.* **103** 073902
[28] Jin C, Wang G, Wei H, Le A T and Lin C 2014 *Nat. Commun.* **5** 4003
[29] Ko D H, Kim K T and Nam C H 2012 *J. Phys. B: At. Mol. Opt. Phys.* **45** 074015
[30] Pabst S and Dahlström J M 2017 *J. Phys. B: At. Mol. Opt. Phys.* **50** 104002
[31] Li J *et al* 2017 *Nat. Commun.* **8** 186
[32] Ishii N, Kaneshima K, Kitano K, Kanai T, Watanabe S and Itatani J 2012 *Opt. Lett.* **37** 4182
[33] Yin Y, Li J, Ren X, Zhao K, Wu Y, Cunningham E and Chang Z 2016 *Opt. Lett.* **41** 1142
[34] Deng Y *et al* 2012 *Opt. Lett.* **37** 4973
[35] Yin Y, Chew A, Ren X, Li J, Wang Y, Wu Y and Chang Z 2017 *Sci. Rep.* **8** 45794
[36] Fuji T and Suzuki T 2007 *Opt. Lett.* **32** 3330
[37] Mirov S, Fedorov V, Moskalev I, Martyshkin D and Kim C 2010 *Laser Photonics Rev.* **4** 21
[38] Schmidt B E *et al* 2010 *Appl. Phys. Lett.* **96** 121109
[39] Cousin S, Silva F, Teichmann S, Hemmer M, Buades B and Biegert J 2014 *Opt. Lett.* **39** 5383
[40] Hong K H, Lai C J, Siqueira J P, Krogen P, Moses J, Chang C L, Stein G J, Zapata L E and Kärtner F X 2014 *Opt. Lett.* **39** 3145
[41] Ishii N, Kaneshima K, Kanai T, Watanabe S and Itatani J 2018 *J. Opt.* **20** 014003
[42] Baltuška A, Fuji T and Kobayashi T 2002 *Phys. Rev. Lett.* **88** 133901
[43] Buchner F, Lübcke A, Heine N and Schultz T 2010 *Rev. Sci. Instrum.* **81** 113107
[44] Zhang Q, Zhao K and Chang Z 2014 *J. Electron Spectrosc. Relat. Phenom.* **195** 48
[45] Saito N, Ishii N, Kanai T, Watanabe S and Itatani J 2016 *Sci. Rep.* **6** 35594
[46] Ishii N, Adachi S, Nomura Y, Kosuge A, Kobayashi Y, Kanai T, Itatani J and Watanabe S 2012 *Opt. Lett.* **37** 97
[47] Hentschel M *et al* 2001 *Nature* **414** 509
[48] Zhao K, Zhang Q, Chini M, Wu Y, Wang X and Chang Z 2012 *Opt. Lett.* **37** 3891
[49] Gaumnitz T, Jain A, Pertot Y, Huppert M, Jordan I, Ardana-Lamas F and Wörner H J 2017 *Opt. Express* **25** 27506

[50] Chini M, Mashiko H, Wang H, Chen S, Yun C, Scott S, Gilbertson S and Chang Z 2009 *Opt. Express* **17** 21459

[51] Protopapas M, Keitel C H and Knight P L 1997 *Rep. Prog. Phys.* **60** 389

[52] Doumy G, Wheeler J, Roedig C, Chirla R, Agostini P and DiMauro L 2009 *Phys. Rev. Lett.* **102** 093002

[53] Chini M, Gilbertson S, Khan S D and Chang Z 2010 *Opt. Express* **18** 13006

[54] Wuilleumier F and Krause M 1974 *Phys. Rev.* A **10** 242

[55] Schultze M *et al* 2010 *Science* **328** 1658

[56] Bizau J and Wuilleumier F 1995 *J. Electron Spectrosc. Relat. Phenom.* **71** 205

[57] Mairesse Y and Quéré F 2005 *Phys. Rev.* A **71** 011401

[58] Kane D J 1999 *IEEE J. Quantum Electron.* **35** 421

[59] Gagnon J, Goulielmakis E and Yakovlev V S 2008 *Appl. Phys.* B **92** 25

[60] Lucchini M, Brügmann M, Ludwig A, Gallmann L, Keller U and Feurer T 2015 *Opt. Express* **23** 29502

[61] Keathley P, Bhardwaj S, Moses J, Laurent G and Kärtner F 2016 *New J. Phys.* **18** 073009

[62] Zhao X, Wei H, Wu Y and Lin C 2017 *Phys. Rev.* A **95** 043407

[63] Remacle F and Levine R 2006 *Proc. Natl Acad. Sci.* **103** 6793

[64] Chini M, Wang X, Cheng Y, Wu Y, Zhao D, Telnov D A, Chu S I and Chang Z 2013 *Sci. Rep.* **3** 1105

[65] Wang H, Chini M, Chen S, Zhang C H, He F, Cheng Y, Wu Y, Thumm U and Chang Z 2010 *Phys. Rev. Lett.* **105** 143002

[66] Tronc M, King G C and Read F 1979 *J. Phys. B: At. Mol. Phys.* **12** 137

[67] Fecko C, Loparo J and Tokmakoff A 2004 *Opt. Commun.* **241** 521

[68] Brida D, Manzoni C, Cirmi G, Marangoni M, De Silvestri S and Cerullo G 2007 *Opt. Express* **15** 15035

[69] Brida D, Marangoni M, Manzoni C, De Silvestri S and Cerullo G 2008 *Opt. Lett.* **33** 2901

[70] Chalus O, Bates P K, Smolarski M and Biegert J 2009 *Opt. Express* **17** 3587

[71] Erny C, Heese C, Haag M, Gallmann L and Keller U 2009 *Opt. Express* **17** 1340

[72] Zhao K, Zhong H, Yuan P, Xie G, Wang J, Ma J and Qian L 2013 *Opt. Lett.* **38** 2159

[73] Andriukaitis G *et al* 2011 *Opt. Lett.* **36** 2755

[74] Yin Y, Li J, Ren X, Wang Y, Chew A and Chang Z 2016 *Opt. Express* **24** 24989

[75] Zhang Q *et al* 2011 *Opt. Express* **19** 7190

[76] Fu Y, Takahashi E J and Midorikawa K 2015 *Opt. Lett.* **40** 5082

[77] Fu Y, Takahashi E J, Zhang Q, Lu P and Midorikawa K 2015 *J. Opt.* **17** 124001

[78] Fu Y, Takahashi E J and Midorikawa K 2017 *IEEE Photonics J.* **9** 1

[79] Wandel S, Lin M W, Yin Y, Xu G and Jovanovic I 2016 *J. Opt. Soc. Am.* B **33** 1580

[80] Hong Z, Zhang Q, Rezvani S A, Lan P and Lu P 2018 *Opt. Laser Technol.* **98** 169

[81] Yin Y, Ren X, Chew A, Li J, Wang Y, Zhuang F, Wu Y and Chang Z 2017 *Sci. Rep.* **7** 11097

[82] Schmidt B E, Thiré N, Boivin M, Laramée A, Poitras F, Lebrun G, Ozaki T, Ibrahim H and Légaré F 2014 *Nat. Commun.* **5** 3643

[83] Shumakova V, Malevich P, Ališauskas S, Voronin A, Zheltikov A, Faccio D, Kartashov D, Baltuška A and Pugžlys A 2016 *Nat. Commun.* **7** 12877

[84] Wandel S, Xu G, Yin Y and Jovanovic I 2014 *J. Phys. B: At. Mol. Opt. Phys.* **47** 234016

[85] Wandel S, Lin M W, Yin Y, Xu G and Jovanovic I 2016 *Opt. Express* **24** 5287

[86] Malevich P, Kanai T, Hoogland H, Holzwarth R, Baltuška A and Pugžlys A 2016 *Opt. Lett.* **41** 930

[87] Sanchez D, Hemmer M, Baudisch M, Cousin S, Zawilski K, Schunemann P, Chalus O, Simon-Boisson C and Biegert J 2016 *Optica* **3** 147

[88] von Grafenstein L, Bock M, Ueberschaer D, Zawilski K, Schunemann P, Griebner U and Elsaesser T 2017 *Opt. Lett.* **42** 3796

[89] Rundquist A, Durfee C G, Chang Z, Herne C, Backus S, Murnane M M and Kapteyn H C 1998 *Science* **280** 1412

[90] Möller M, Cheng Y, Khan S D, Zhao B, Zhao K, Chini M, Paulus G G and Chang Z 2012 *Phys. Rev.* A **86** 011401

[91] Laurent G, Cao W, Li H, Wang Z, Ben-Itzhak I and Cocke C L 2012 *Phys. Rev. Lett.* **109** 083001

[92] Ko D H, Kim K T, Park J, Lee J h and Nam C H 2010 *New J. Phys.* **12** 063008

[93] Zheng Y, Zeng Z, Zou P, Zhang L, Li X, Liu P, Li R and Xu Z 2009 *Phys. Rev. Lett.* **103** 043904